

# **Histogram-free reweighting with grand canonical Monte Carlo: Post-simulation optimization of non-bonded potentials for phase equilibria**

Richard A. Messerly,<sup>\*,†</sup> Mohammad Soroush Barhaghi,<sup>‡</sup> Jeffrey J. Potoff,<sup>‡</sup>  
and Michael R. Shirts<sup>¶</sup>

<sup>†</sup>*Thermodynamics Research Center, National Institute of Standards and Technology, Boulder,  
Colorado, 80305, United States*

<sup>‡</sup>*Department of Chemical Engineering and Materials Science, Wayne State University, Detroit,  
Michigan 48202, United States*

<sup>¶</sup>*Department of Chemical and Biological Engineering, University of Colorado Boulder, Colorado,  
80309, United States*

E-mail: richard.messerly@nist.gov

# Abstract

Histogram reweighting (HR) is a standard approach for converting grand canonical Monte Carlo (GCMC) simulation output into vapor-liquid coexistence properties (saturated liquid density,  $\rho_{\text{liq}}^{\text{sat}}$ , saturated vapor density,  $\rho_{\text{vap}}^{\text{sat}}$ , saturated vapor pressures,  $P_{\text{vap}}^{\text{sat}}$ , and enthalpy of vaporization,  $\Delta H_v$ ). We demonstrate that a histogram-free reweighting approach, namely, the Multistate Bennett Acceptance Ratio (MBAR), is similar to the traditional HR method for computing  $\rho_{\text{liq}}^{\text{sat}}$ ,  $\rho_{\text{vap}}^{\text{sat}}$ ,  $P_{\text{vap}}^{\text{sat}}$ , and  $\Delta H_v$ . The primary advantage of MBAR is the ability to predict phase equilibria properties for an arbitrary force field parameter set that has not been simulated directly. Thus, MBAR can greatly reduce the number of GCMC simulations that are required to parameterize a force field with phase equilibria data.

Four different applications of GCMC-MBAR are presented in this study. First, we validate that GCMC-MBAR and GCMC-HR yield statistically indistinguishable results for  $\rho_{\text{liq}}^{\text{sat}}$ ,  $\rho_{\text{vap}}^{\text{sat}}$ ,  $P_{\text{vap}}^{\text{sat}}$ , and  $\Delta H_v$  in a limiting test case. Second, we utilize GCMC-MBAR to optimize an individualized (compound-specific) parameter ( $\psi$ ) for 8 branched alkanes and 11 alkynes using the Mie Potentials for Phase Equilibria (MiPPE) force field. Third, we predict  $\rho_{\text{liq}}^{\text{sat}}$ ,  $\rho_{\text{vap}}^{\text{sat}}$ ,  $P_{\text{vap}}^{\text{sat}}$ , and  $\Delta H_v$  for force field  $j$  by simulating force field  $i$ , where  $i$  and  $j$  are common force fields from the literature. In addition, we provide guidelines for determining the reliability of GCMC-MBAR predicted values. Fourth, we develop and apply a post-simulation optimization scheme to obtain new MiPPE non-bonded parameters for cyclohexane ( $\epsilon_{\text{CH}_2}$ ,  $\sigma_{\text{CH}_2}$ , and  $\lambda_{\text{CH}_2}$ ).

# 1 Introduction

A key use of molecular simulation is the ability to accurately and efficiently estimate vapor-liquid phase equilibria properties, i.e., saturated liquid density ( $\rho_{\text{liq}}^{\text{sat}}$ ), saturated vapor density ( $\rho_{\text{vap}}^{\text{sat}}$ ), saturated vapor pressures ( $P_{\text{vap}}^{\text{sat}}$ ), and enthalpy of vaporization ( $\Delta H_v$ ). The accuracy of coexistence estimates depends on the underlying molecular model (a.k.a., force field, potential model, or Hamiltonian) while the computational efficiency depends primarily on the simulation methods, software, and hardware.

Several simulation approaches exist for computing vapor-liquid coexistence properties.<sup>1</sup> These include Gibbs Ensemble Monte Carlo (GEMC),<sup>1,2</sup> grand canonical Monte Carlo coupled with histogram reweighting (GCMC-HR),<sup>1-3</sup> two-phase molecular dynamics (2 $\phi$ MD),<sup>4</sup> and isothermal-isochoric integration (ITIC).<sup>5</sup> The improved efficiency of these methods has greatly enabled the development of accurate force fields.<sup>6-10</sup> However, parameterization of non-bonded interactions with vapor-liquid coexistence calculations over a wide range of temperatures remains an arduous and time-consuming task. For example, recent studies have implemented an exhaustive grid-based search optimization by performing GCMC-HR simulations with hundreds of non-bonded parameter sets.<sup>11-13</sup>

The primary motivation for this work is to reduce the computational cost of optimizing non-bonded parameters with vapor-liquid phase equilibria properties. This is achieved by substituting histogram reweighting with the Multistate Bennett Acceptance Ratio (MBAR),<sup>14,15</sup> a histogram-free reweighting schema. The proposed GCMC-MBAR method is identical to the traditional GCMC-HR approach except that MBAR reweights configurations rather than histograms. The benefit of this simple modification is that GCMC-MBAR can estimate phase equilibria for non-bonded parameter sets that have not been simulated directly. While storing configuration files is significantly more memory intensive than storing histogram files, this additional storage load can be alleviated

greatly by utilizing basis functions (see Section 2.4).

In related studies, Messerly et al. demonstrate how to combine MBAR with ITIC (MBAR-ITIC) to optimize generalized Lennard-Jones (Mie  $\lambda$ -6) potentials.<sup>16,17</sup> For MBAR-ITIC, a series of simulations are performed with a constant number of molecules, constant volume, and constant temperature ( $NVT$ ) along a supercritical isotherm and liquid density isochore(s) with a “reference” force field(s) ( $\theta_{\text{ref}}$ ). Subsequently, the energies and forces are recomputed for the configurations sampled with  $\theta_{\text{ref}}$  using a different “rerun” force field ( $\theta_{\text{rr}}$ ). MBAR reweights the reference configurations to estimate the internal energy ( $U$ ) and pressure ( $P$ ) at each  $(T, \rho)$  state point for  $\theta_{\text{rr}}$ , without directly running simulations with  $\theta_{\text{rr}}$ . ITIC then converts the MBAR  $U$  and  $P$  estimates into vapor-liquid phase equilibria properties for  $\theta_{\text{rr}}$ .<sup>5,18</sup>

The results from Messerly et al. demonstrate that MBAR-ITIC is most reliable in the local domain, i.e., when  $\theta_{\text{rr}} \approx \theta_{\text{ref}}$ .<sup>16</sup> Furthermore, MBAR-ITIC performs best for changes in the non-bonded well-depth parameter ( $\epsilon$ ) while it performs significantly worse for large changes in the non-bonded size ( $\sigma$ ) and repulsive exponent ( $\lambda$ ) parameters. Because molecular configurations in condensed phases depend strongly on short-range interactions, this poor “overlap” is primarily observed when  $\sigma_{\text{rr}} \not\approx \sigma_{\text{ref}}$  or  $\lambda_{\text{rr}} \not\approx \lambda_{\text{ref}}$ . The degree of overlap can be quantified by the number of effective snapshots ( $K_{\text{snaps}}^{\text{eff}}$ ), which is essentially the number of non-negligible configurations that contribute to the estimated ensemble averages. Poor overlap (low  $K_{\text{snaps}}^{\text{eff}}$ ) is especially problematic for MBAR-ITIC as a large number of snapshots is needed to obtain precise estimates of  $P$  in the liquid phase, due to large fluctuations in  $P$  at high densities.

Our initial hypothesis was that GCMC-MBAR would experience better overlap than was observed for MBAR-ITIC when  $\theta_{\text{rr}} \not\approx \theta_{\text{ref}}$ . There were two main reasons for this hypothesis. First, as opposed to the fixed density  $NVT$  simulations used in ITIC, GCMC simulations sample from a wider range of configurations and energies. Second, ITIC re-

quires larger box sizes (and, thereby, more molecules) than those typically utilized with GCMC. By utilizing fewer molecules, GCMC simulations experience larger energy fluctuations (on a percent basis) which improves the overlap between states. We also hypothesized that the impact of poor overlap would be less severe compared to MBAR-ITIC, where poor overlap leads to sporadic values of  $P$  and nonsensical phase equilibria estimates.

The method outlined in this study is similar in spirit to “Hamiltonian scaling” (HS), which has been applied to both GEMC<sup>19</sup> and GCMC simulations.<sup>1,20–22</sup> The HS approach samples from multiple force fields (Hamiltonians) in a single simulation according to a weighted sampling probability. A separate histogram is stored for each  $\theta_{\text{ref}}$  by scaling the fractional contribution of the combined histogram from all reference force fields. Vapor-liquid phase equilibria properties for each  $\theta_{\text{ref}}$  are estimated post-simulation by applying traditional histogram reweighting to the respective scaled histograms. For the GCMC implementation of Hamiltonian scaling (HS-GCMC),  $\mu$  and  $T$  are not stationary during the simulation, rather the current values of  $\mu$  and  $T$  depend on which  $\theta_{\text{ref}}$  is being sampled.

Despite HS-GCMC proving to be a powerful tool to optimize force field parameters,<sup>1,20–22</sup> it has yet to gain widespread popularity. This is likely due to the added complexity of both the simulation protocol and the histogram post-processing. Also, HS requires that a decision be made *a priori* regarding which force fields are to be tested. By contrast, GCMC-MBAR does not require any modification of the simulation procedure, the post-processing is essentially unchanged compared to traditional histogram reweighting, and the non-bonded parameter sets need not be selected prior to the simulations. This final distinction is of utmost importance as GCMC-MBAR is capable of predicting phase equilibria post-simulation for any force field parameter set ( $\theta_{\text{rr}} = \theta_{\text{ref}}$  and  $\theta_{\text{rr}} \neq \theta_{\text{ref}}$ ), whereas HS-GCMC can predict phase equilibria only for the parameter sets that are tested at run time.

The outline for this study is the following. Section 2 provides details regarding the force fields, simulation set-up, and the HR/MBAR post-simulation analysis. Section 3 presents results of GCMC-MBAR for four scenarios. Section 3.1 validates that GCMC-MBAR and GCMC-HR yield indistinguishable coexistence estimates for a fixed force field. Section 3.2 applies GCMC-MBAR to a recently proposed  $\epsilon$ -scaling approach. Section 3.3 shows how GCMC-MBAR can predict coexistence properties for force field  $j$  by reweighting configurations sampled with force field  $i$ . Section 3.4 demonstrates how GCMC-MBAR can be utilized to rapidly optimize the united-atom Mie  $\lambda$ -6 parameters for cyclohexane. Section 4 discusses some limitations and provides recommendations for future work. Section 5 reviews the primary conclusions.

## 2 Methods

### 2.1 Force fields

The force fields utilized in this study are Mie Potentials for Phase Equilibria (MiPPE),<sup>8,12,13</sup> Transferable Potentials for Phase Equilibria (TraPPE-UA, referred to simply as TraPPE<sup>6,23,24</sup>), and Nath, Escobedo, and de Pablo revised (NERD).<sup>25,26</sup> Each force field adopts a united-atom (UA) representation, where non-polar hydrogens are not modeled explicitly.

We employ fixed bond lengths for each force field studied. Note that this is inconsistent with the original NERD force field, which was developed using a harmonic bond potential. The primary reason we utilize fixed bond lengths for the NERD potential is to allow for a valid comparison of our GCMC-MBAR values with the GCMC-HR results of Mick et al.,<sup>12</sup> which were also obtained using fixed bonds. Fixed bonds are also more computationally efficient in Monte Carlo simulations and, in addition, flexible bonds are not yet supported by the simulation package utilized in this study (see Section 2.2). Fur-

thermore, Section S2 of Supporting Information demonstrates that the branched alkane NERD phase equilibria results obtained with fixed bonds (as reported by Mick et al.<sup>12</sup>) agree with the flexible-bond results (as reported by Nath et al.<sup>26</sup>).

Angular bending interactions for each force field are evaluated using a harmonic potential:

$$u^{\text{bend}} = \frac{k_{\theta}}{2} (\theta - \theta_{\text{eq}})^2 \quad (1)$$

where  $u^{\text{bend}}$  is the bending energy,  $\theta$  is the instantaneous bond angle,  $\theta_{\text{eq}}$  is the equilibrium bond angle, and  $k_{\theta}$  is the harmonic force constant.

Dihedral torsional interactions for each force field are determined using a cosine series:

$$u^{\text{tors}} = c_0 + c_1 (1 + \cos \phi) + c_2 (1 - \cos 2\phi) + c_3 (1 + \cos 3\phi) \quad (2)$$

where  $u^{\text{tors}}$  is the torsional energy,  $\phi$  is the dihedral angle and  $c_n$  are the Fourier constants. Bond lengths,  $\theta_{\text{eq}}$ ,  $k_{\theta}$ , and  $c_n$  values for each force field are reported in Section S1 of Supporting Information.

In accordance with Reference 27, we simulate cyclohexane using the TraPPE  $\text{CH}_x\text{-CH}_2\text{-CH}_2\text{-CH}_y$  torsional parameters instead of the TraPPE C-C-C-C six-member ring torsional parameters reported in Table 3 of Reference 24. This choice is made to better replicate the vapor-liquid coexistence densities reported in Reference 24, as we suspect there is a typographical error in Reference 24 for the TraPPE C-C-C-C six-member ring torsional potential. Note that, subsequent to submitting this manuscript, an alternative equation to Equation 2 is now provided on the official TraPPE website<sup>28</sup> for the cyclohexane torsional potential (although we are still wary of a possible sign error for the  $c_1$  term).

Non-bonded interactions between sites located in two different molecules or separated by more than three bonds within the same molecule are calculated using a Mie  $\lambda$ -6

potential (of which the Lennard-Jones, LJ, 12-6 is a subclass):

$$u^{\text{nb}}(\epsilon, \sigma, \lambda; r) = \left( \frac{\lambda}{\lambda - 6} \right) \left( \frac{\lambda}{6} \right)^{\frac{6}{\lambda - 6}} \epsilon \left[ \left( \frac{\sigma}{r} \right)^{\lambda} - \left( \frac{\sigma}{r} \right)^6 \right] \quad (3)$$

where  $u^{\text{nb}}$  is the non-bonded energy,  $\sigma$  is the distance ( $r$ ) where  $u^{\text{nb}} = 0$ ,  $-\epsilon$  is the energy of the potential at the minimum (i.e.,  $u^{\text{nb}} = -\epsilon$  and  $\frac{\partial u^{\text{nb}}}{\partial r} = 0$  for  $r = r_{\text{min}}$ ), and  $\lambda$  is the repulsive exponent. Note that Coulombic (electrostatic) interactions are not computed because the MiPPE, TraPPE, and NERD force fields do not include charges for any of the compounds studied.

The non-bonded Mie  $\lambda$ -6 force field parameters for MiPPE, TraPPE, and NERD are provided in Table 1. MiPPE reports a “generalized” (MiPPE-gen) and “short/long” (MiPPE-SL) CH and C parameter set. The “short” and “long” parameters are implemented when the number of carbons in the backbone is  $\leq 4$  and  $> 4$ , respectively. Also note that the NERD force field has several different  $\text{CH}_3$  non-bonded parameter sets.

Non-bonded parameters between two different site types (i.e., cross-interactions) are determined using Lorentz-Berthelot combining rules<sup>29</sup> for  $\epsilon$  and  $\sigma$  and an arithmetic mean for the repulsive exponent  $\lambda$  (as recommended in Reference 8):

$$\epsilon_{ij} = \sqrt{\epsilon_{ii}\epsilon_{jj}} \quad (4)$$

$$\sigma_{ij} = \frac{\sigma_{ii} + \sigma_{jj}}{2} \quad (5)$$

$$\lambda_{ij} = \frac{\lambda_{ii} + \lambda_{jj}}{2} \quad (6)$$

where the  $ij$  subscript refers to cross-interactions and the subscripts  $ii$  and  $jj$  refer to same-site interactions.



Table 1: Non-bonded (Mie  $\lambda$ -6) parameters for TraPPE,<sup>6,23,24</sup> MiPPE,<sup>8,12,13</sup> and NERD.<sup>25,26</sup>

United-atom	$\epsilon/k_B$ (K)	$\sigma$ (nm)	$\lambda$
MiPPE			
CH <sub>3</sub>	121.25	0.3783	16
CH <sub>2</sub> (sp <sup>3</sup> )	61	0.399	16
CH(sp <sup>3</sup> ), gen.	15	0.46	16
C(sp <sup>3</sup> ), gen.	1.2	0.61	16
CH(sp <sup>3</sup> ), short	15	0.47	16
C(sp <sup>3</sup> ), short	1.45	0.61	16
CH(sp <sup>3</sup> ), long	14	0.47	16
C(sp <sup>3</sup> ), long	1.2	0.62	16
CH(sp)	148.5	0.357	28
C(sp) (1-alkyne)	206	0.2875	16
C(sp) (2-alkyne)	118	0.312	16
CH <sub>2</sub> (cyclohexane) <sup>a</sup>	69.7	0.3902	16
TraPPE			
CH <sub>3</sub>	98	0.375	12
CH <sub>2</sub> (sp <sup>3</sup> )	46	0.395	12
CH(sp <sup>3</sup> )	10	0.468	12
C(sp <sup>3</sup> )	0.5	0.640	12
CH <sub>2</sub> (cyclohexane)	52.5	0.391	12
NERD			
CH <sub>3</sub> (general)	104.00	0.391	12
CH <sub>3</sub> (2-methylpropane)	78.23	0.388	12
CH <sub>3</sub> (2,2-dimethylpropane)	74.50	0.391	12
CH <sub>3</sub> (methyl side chain)	70.00	0.385	12
CH <sub>3</sub> (ethyl side chain)	83.00	0.382	12
CH <sub>2</sub> (sp <sup>3</sup> )	45.80	0.393	12
CH(sp <sup>3</sup> )	39.70	0.385	12
C(sp <sup>3</sup> )	17.00	0.391	12
<sup>a</sup> This work. See Section 3.4			

## 2.2 Simulation set-up

The results presented in Sections 3.1 and 3.2 are obtained by reprocessing simulation output that were analyzed in previous studies with histogram reweighting.<sup>12,13</sup> New simulation results are provided in Sections 3.3 and 3.4 for 2-methylpropane, 2,2-dimethylpropane,

2,2-dimethylbutane, 3,3-dimethylhexane, 3-methyl-3-ethylpentane, 2,2,4-trimethylhexane, 2,3-dimethylbutane, 2,3,4-trimethylpentane, and cyclohexane.

Each compound is simulated with grand canonical Monte Carlo (GCMC), i.e., constant chemical potential ( $\mu$ ), volume ( $V$ ), and temperature ( $T$ ). A series of nine GCMC simulations are performed, two in the vapor phase, six in the liquid phase (with a temperature spacing of approximately 20 K), and one near critical which acts as the “bridge” between the vapor and liquid phases. A single simulation is performed at each state point ( $\mu, V, T$ ), with the exception of the MiPPE cyclohexane results, which are obtained from 20 independent replicate simulations.

The system volume is constant for a given compound. The cubic box side length is 3 nm for 2-methylpropane, 2,2-dimethylpropane, 2,3-dimethylbutane, and cyclohexane, 3.5 nm for 2,3,4-trimethylpentane and 3,3-dimethylhexane, and 4 nm for 2,2,4-trimethylhexane and 3-methyl-3-ethylpentane. The prescribed  $\mu$ ,  $T$ , and  $V$  values for the branched alkanes are the same as those utilized in Mick et al. and vary somewhat between force fields.<sup>12</sup> All simulated state points ( $\mu, V, T$ ) are reported in Section S9 of Supporting Information.

A low-density (less than twenty molecules) initial configuration is utilized for the vapor phase simulations, while the bridge and liquid phase simulations are initialized with a high-density (around 150 molecules) configuration. To verify that finite size effects are negligible in the low-density vapor phase, we confirm that the saturated vapor compressibility factor ( $Z_{\text{vap}}^{\text{sat}}$ ) converges smoothly to 1 for each compound (see Section S7 of Supporting Information).<sup>30</sup>

Each GCMC simulation performed in this study consists of an equilibration and production stage of  $2 \times 10^7$  and  $2.5 \times 10^7$  Monte Carlo steps (MCS), respectively. Snapshots (i.e., number of molecules, internal energy, and optionally the xyz coordinates) are stored every 200 MCS to reduce the correlation between sequential configurations. Thus, the number of snapshots ( $K_{\text{snaps}}$ ) for a single state point ( $\mu, V, T$ ) is  $1.25 \times 10^5$ .

Displacement and rotation moves are required to thermally equilibrate the system at the simulation temperature while molecule insertion and deletion moves ensure that  $\mu$  is equal to the prescribed value. Cyclohexane simulations also employ crank-shaft moves to sample internal configurations, which can be challenging for ring molecules.<sup>31,32</sup> The type of Monte Carlo move implemented for each step is selected randomly. The displacement, rotation, and molecule swap move probabilities for branched alkanes are 30%, 10%, and 60%, respectively. The move probabilities for cyclohexane are 30%, 10%, 40%, and 20% for displacement, rotation, molecule swap, and crank-shaft moves, respectively.

All simulations utilize coupled-decoupled configurational-bias Monte Carlo (CBMC)<sup>23</sup> to enhance the insertion acceptance rate, with 100 angle trials, 30 dihedral trials, 10 initial site trials, and 4 subsequent site trials. The move probabilities are consistent with those of Mick et al. and Soroush Barhaghi et al.,<sup>12,13</sup> while the CBMC dihedral trials and initial site trials differ slightly. Section S3 provides an example of the CBMC acceptance rates for the different simulation state points.

Consistent with previous MiPPE studies,<sup>8,12,13</sup> we utilize a 1.0 nm non-bonded cut-off distance with analytical tail corrections for internal energy.<sup>29</sup> Although TraPPE<sup>6,23,24</sup> and NERD<sup>25,26</sup> were parameterized using a 1.4 nm and 1.38 nm cut-off, respectively, we compare our TraPPE and NERD validation results with those from Mick et al.,<sup>12</sup> which also utilizes a 1.0 nm cut-off.

All simulations are performed using GPU optimized Monte Carlo (GOMC)<sup>33</sup> development version. Although GOMC is capable of implementing graphics processing units (GPUs), all simulations are performed with central processing units (CPUs) because of the relatively simple systems that are studied (i.e., small box sizes and no electrostatics). A description of the compiler and machine hardware is provided in Section S4 of Supporting Information.

Initial configurations are generated with Packmol,<sup>34</sup> while psfgen is used to generate

the coordinate (\*.pdb) and connectivity (\*.psf) files.<sup>35</sup> Example GOMC input files with corresponding shell and Python scripts for preparing, running, and analyzing simulations are provided at [https://github.com/ramess101/MBAR\\_GCMC](https://github.com/ramess101/MBAR_GCMC).

## 2.3 Comparison between GCMC-MBAR and GCMC-HR

Converting the GCMC simulation output into vapor-liquid phase equilibria properties requires significant post-processing through reweighting. Histogram reweighting (HR) and, more generally, configuration reweighting is an important tool in many fields of molecular simulation.<sup>36,37</sup> In fact, it has long since been known that it is possible to estimate properties for state  $j$  by reweighting configurations that were sampled with state  $i$ .<sup>1,38–40</sup>

For example, umbrella sampling simulations are often processed using the weighted histogram analysis method (WHAM) to compute free energy differences between states.<sup>41</sup> WHAM (or HR) is essentially an approximation of MBAR and, therefore, MBAR should be favored for free energy calculations whenever a histogram-free approach is feasible.<sup>42,43</sup> In this study, we implement MBAR in Python 2.7 through the *pymbar* package available at <https://github.com/choderalab/pymbar>.

Before demonstrating how to compute vapor-liquid phase equilibria with GCMC-MBAR in Sections 2.3.2 and 2.3.4, we review the traditional GCMC-HR approach in Section 2.3.1. We also discuss the steps of this procedure that are the same for both GCMC-HR and GCMC-MBAR in Section 2.3.3. We refer the interested reader to the literature for derivations and more detailed discussion of the GCMC-HR equations (cf. Reference 1).

### 2.3.1 Histogram reweighting

Histogram reweighting computes the ensemble average of a given observable ( $O$ , e.g.,  $U$  and  $\rho$ ) according to

$$\langle O(\mu, \beta) \rangle = \sum_U \sum_N O \times Pr(N, U; \mu, \beta) \quad (7)$$

where  $\langle \dots \rangle$  denotes an ensemble average and  $Pr(N, U; \mu, \beta)$  is the probability of observing  $N$  molecules with internal energy  $U$  for a given chemical potential ( $\mu$ ) and inverse temperature ( $\beta \equiv \frac{1}{k_B T}$ , where  $k_B$  is the Boltzmann constant). The double summation is computed numerically where  $U$  and  $N$  are discretized into a 2-dimensional histogram. The probability is obtained with HR from<sup>36,37</sup>

$$Pr(N, U; \mu, \beta) = \frac{\sum_{i=1}^R K_{\text{snaps},i}(N, U) \exp(-\beta U + \beta \mu N)}{\sum_{i=1}^R K_{\text{snaps},i} \exp(-\beta_i U + \beta_i \mu_i N + \hat{f}_i)} \quad (8)$$

where  $R$  is the number of runs,  $K_{\text{snaps},i}(N, U)$  is the number of (uncorrelated) configuration “snapshots” in the  $i^{\text{th}}$  run (with  $\beta_i$  and  $\mu_i$ ) that have  $N$  molecules and  $U$  within the histogram bin width,  $K_{\text{snaps},i}$  is the total number of snapshots for run  $i$  (i.e.,  $K_{\text{snaps},i} = \sum_{N,U} K_{\text{snaps},i}(N, U)$ ), and  $\hat{f}_i$  is an estimate for the reduced free energy, which is calculated with the relationship

$$\hat{f}(\mu, \beta) = -\ln \sum_U \sum_N \frac{\sum_{i=1}^R K_{\text{snaps},i}(N, U) \exp(-\beta U + \beta \mu N)}{\sum_{i=1}^R K_{\text{snaps},i} \exp(-\beta_i U + \beta_i \mu_i N + \hat{f}_i)} \quad (9)$$

where  $\hat{f}_i \equiv \hat{f}(\mu_i, \beta_i)$ . Note that because  $\hat{f}_i$  can also be viewed simply as a constant that solves the self-consistent equations, the GCMC-HR literature<sup>1</sup> typically adopts the notation  $C_i$  (or more specifically,  $-C_i$ ) instead of  $\hat{f}_i$ . We prefer  $\hat{f}_i$  for a clear comparison with the MBAR expressions that follow.

### 2.3.2 Histogram-free reweighting

Equations 7, 8, and 9 only allow for reweighting simulations at a different  $\beta$  and  $\mu$ . By contrast, MBAR can also be applied to reweight simulations for different force field parameters ( $\theta$ ). The analogous MBAR equation to Equation 7 is

$$\langle O(\theta, \mu, \beta) \rangle = \sum_{n=1}^{K_{\text{snaps}}^{\text{tot}}} O(\mathbf{x}_n, N_n; \theta, \mu, \beta) \times W_n(\theta, \mu, \beta) \quad (10)$$

where  $(\mathbf{x}_n, N_n)$  are *uncorrelated* configurations sampled from  $i = 1 \dots R$  simulations at inverse temperature ( $\beta_i$ ), chemical potential ( $\mu_i$ ), and reference force field parameters ( $\theta_{\text{ref},i}$ ), and  $K_{\text{snaps}}^{\text{tot}} \equiv \sum_{i=1}^R K_{\text{snaps},i}$  is the total number of snapshots for all  $R$  runs.  $W_n(\theta, \beta, \mu)$  is the weight of the  $n^{\text{th}}$  configuration for an arbitrary  $\mu$ ,  $\beta$ , and  $\theta$ .  $W_n$  is computed with the following expression (analogous to Equation 8)

$$W_n(\theta, \beta, \mu) = \frac{\exp[\hat{f}(\theta, \beta, \mu) - u(\mathbf{x}_n, N_n; \theta, \beta, \mu)]}{\sum_{i=1}^R K_{\text{snaps},i} \exp[\hat{f}(\theta_i, \beta_i, \mu_i) - u(\mathbf{x}_n, N_n; \theta_i, \beta_i, \mu_i)]} \quad (11)$$

where  $u(\mathbf{x}_n, N_n; \theta, \beta, \mu)$  is the reduced potential energy evaluated with  $\theta$ ,  $\beta$ , and  $\mu$  for configuration  $(\mathbf{x}_n, N_n)$ . The reduced free energy is computed with an expression analogous to Equation 9

$$\hat{f}(\theta, \beta, \mu) = -\ln \sum_{n=1}^{K_{\text{snaps}}^{\text{tot}}} \frac{\exp[-u(\mathbf{x}_n, N_n; \theta, \beta, \mu)]}{\sum_{i=1}^R K_{\text{snaps},i} \exp[\hat{f}(\theta_i, \beta_i, \mu_i) - u(\mathbf{x}_n, N_n; \theta_i, \beta_i, \mu_i)]} \quad (12)$$

For the grand canonical ensemble, the reduced potential energy is

$$u(\mathbf{x}_n, N_n; \theta, \beta, \mu) = \beta U(\mathbf{x}_n, N_n; \theta) - \beta \mu N_n \quad (13)$$

### 2.3.3 Comparison between HR and MBAR

The similarities between MBAR (Equations 11 and 12) and HR (Equations 8 and 9) are readily apparent after substituting Equation 13 into Equations 11 and 12. Indeed, the difference between HR and MBAR is primarily that of bookkeeping, although the histogram-free approach of MBAR does have some benefits when varying force field parameters, as discussed below.

In the histogram context, snapshots with similar  $U(\theta_{\text{ref}})$  would not necessarily belong in the same  $U$  histogram bin when recomputed with a different force field. Similarly, we cannot easily separate out snapshots in the same  $U$  histogram that were performed with multiple  $\theta_{\text{ref}}$ . However, if we perform sums over snapshots, we can carry out simulations at different force field parameters ( $\theta_{\text{ref},i}$ ). Furthermore, we can reevaluate the configurational energy ( $U(\mathbf{x}_n, N_n; \theta_{\text{rr}})$ ) with a range of different parameters for the relatively small expense of rerunning only a subset of uncorrelated snapshots with  $\theta_{\text{rr}}$ .

If, however, all  $R$  simulations are performed with a single reference force field ( $\theta_{\text{ref}}$ ) and  $\theta_{\text{rr}} = \theta_{\text{ref}}$ , these two sets of equations (HR: Equations 7, 8, and 9, MBAR: Equations 10, 11, and 12) can be seen as equivalent in the limit of infinitesimal histogram bin widths. In the zero bin width limit, no histogram contains more than 1 snapshot and, therefore,  $U$  and  $N$  for each histogram can be taken to be the  $U(\mathbf{x}_n, N_n)$  and  $N_n$  of the single observation in that histogram, while histograms with no snapshots can be omitted. Thus,  $K_{\text{snaps},i}(N, U)$  is either 1 or 0, and the sum over all histograms becomes a sum over snapshots conducted in all  $R$  simulation runs. Equations 8 and 9 then reduce to Equations 11 and 12, respectively.

Both HR and MBAR require solving a system of  $R - 1$  nonlinear equations for self-consistency (Equations 8 and 9 for HR and Equations 11 and 12 for MBAR). Specifically, initial guesses for  $\hat{f}_i$  are updated iteratively until convergence. There is provably only one solution,<sup>15</sup> so as long as certain criteria are met that will be discussed below. Thus,

although a range of different solver methods exist, the only difference is efficiency and numerical stability.

### 2.3.4 Computing phase equilibria

For both GCMC-HR and GCMC-MBAR, the pressure is computed from

$$P(\theta, \beta, \mu) = \frac{k_B T}{V} \ln \Xi + B = \hat{f}(\theta, \beta, \mu) + B \quad (14)$$

where  $\Xi$  is the grand canonical partition function and  $B$  is an additive constant, which is determined by fitting a straight line to  $\ln \Xi$  with respect to  $N$  at very low densities. At these low densities, the system is assumed to behave as an ideal gas and, therefore, the slope is unity and  $B = \frac{k_B T}{V} \times b$ , where  $b$  is the y-intercept from the straight line regression.

Having determined  $B$ , the saturated vapor pressure ( $P_{\text{vap}}^{\text{sat}}$ ) is computed with Equation 14 at the desired saturation temperature ( $T^{\text{sat}}$ ) and corresponding saturation chemical potential ( $\mu^{\text{sat}}$ ).  $\mu^{\text{sat}}$  is obtained by equating the pressures in the vapor and liquid phases at a fixed value of  $T^{\text{sat}}$ . This is done by integrating  $Pr$  (HR) or  $W_n$  (MBAR) for the two phases separately, i.e., by dividing the snapshots into low and high density regimes. For example, the equality of pressures is satisfied for HR when

$$\sum_U \sum_{N > N_c} Pr(N, U; \mu^{\text{sat}}, \beta^{\text{sat}}) = \sum_U \sum_{N \leq N_c} Pr(N, U; \mu^{\text{sat}}, \beta^{\text{sat}}) \quad (15)$$

where  $N_c$  is an estimate for the number of molecules at the critical density, which serves to distinguish between snapshots that are in the vapor or liquid phases. The analogous MBAR equation is

$$\sum_{n=1}^{K_{\text{snaps}}^{\text{liq}}} W_n(\theta, \beta^{\text{sat}}, \mu^{\text{sat}}) = \sum_{n=1}^{K_{\text{snaps}}^{\text{vap}}} W_n(\theta, \beta^{\text{sat}}, \mu^{\text{sat}}) \quad (16)$$



where  $K_{\text{snaps}}^{\text{liq}}$  and  $K_{\text{snaps}}^{\text{vap}}$  are the number of liquid and vapor snapshots, respectively.

By solving Equations 15 (HR) or 16 (MBAR) for  $\mu^{\text{sat}}$ , the vapor and liquid saturation densities and energies ( $\rho_{\text{liq}}^{\text{sat}}$ ,  $\rho_{\text{vap}}^{\text{sat}}$ ,  $U_{\text{liq}}^{\text{sat}}$ , and  $U_{\text{vap}}^{\text{sat}}$ ) are also computed with a modified version of Equations 7 (HR) or 10 (MBAR), where only snapshots from the desired phase are included in the weighted average. For example, when computing  $\rho_{\text{liq}}^{\text{sat}}$  and  $U_{\text{liq}}^{\text{sat}}$ , the double summation in Equation 7 (HR) is performed only for  $N > N_c$  and the sum in Equation 10 (MBAR) is only over  $K_{\text{snaps}}^{\text{liq}}$  liquid snapshots.

Having computed the pressure, internal energies, and densities for the saturated vapor and saturated liquid, the enthalpy of vaporization is calculated with

$$\Delta H_v = \bar{U}_{\text{vap}}^{\text{sat}} - \bar{U}_{\text{liq}}^{\text{sat}} + P_{\text{vap}}^{\text{sat}}(\bar{V}_{\text{vap}}^{\text{sat}} - \bar{V}_{\text{liq}}^{\text{sat}}) \quad (17)$$

where  $\bar{U}$  and  $\bar{V}$  denote molar energy and molar volume, respectively.

### 2.3.5 Uncertainties in phase equilibria

All uncertainties in this study are reported at the 95% confidence level. Unless otherwise stated, uncertainties for  $\rho_{\text{liq}}^{\text{sat}}$ ,  $\rho_{\text{vap}}^{\text{sat}}$ ,  $P_{\text{vap}}^{\text{sat}}$ ,  $\Delta H_v$ , and  $Z_{\text{vap}}^{\text{sat}}$  are determined with the following bootstrap re-sampling analysis:<sup>44</sup>

1. Perform set of GCMC simulations with single replicate at each state point  $(\mu, V, T)$
2. Randomly select (with replacement) a subset of the  $K_{\text{snaps}}^{\text{tot}}$  snapshots from Step 1
3. Compute phase equilibria for random subset of Step 2 following procedure outlined in Sections 2.3.2 and 2.3.4
4. Repeat Steps 2 and 3  $N_{\text{sets}}$  times, where  $N_{\text{sets}} = 100$  in this study
5. Generate distribution from  $N_{\text{sets}}$  values of  $\rho_{\text{liq}}^{\text{sat}}$ ,  $\rho_{\text{vap}}^{\text{sat}}$ ,  $P_{\text{vap}}^{\text{sat}}$ ,  $\Delta H_v$ , and  $Z_{\text{vap}}^{\text{sat}}$

6. Determine interval that excludes the lowest and highest  $0.025 \times N_{\text{sets}}$  values of distribution

Note that it is important to compute the uncertainties for  $\Delta H_v$  and  $Z_{\text{vap}}^{\text{sat}}$  directly, rather than applying standard propagation of errors methods that typically neglect the correlation between properties.<sup>45</sup>

### 2.3.6 Number of effective snapshots

The performance of HR and MBAR depends primarily on good phase space overlap. For HR, good overlap means that the different sets of simulated  $T$  and  $\mu$  sample configurations and densities that are representative of the vapor and liquid phases at  $T^{\text{sat}}$  and  $\mu^{\text{sat}}$ . For MBAR, an additional requirement is that the configurations sampled with  $\theta_{\text{ref}}$  also represent feasible configurations for  $\theta_{\text{rr}}$ .<sup>16,46</sup> The amount of overlap can be quantified by the number of effective snapshots ( $K_{\text{snaps}}^{\text{eff}}$ ),<sup>47</sup> using Kish's formula:

$$K_{\text{snaps}}^{\text{eff}} = \frac{(\sum_n W_n)^2}{\sum_n W_n^2} \quad (18)$$

which reduces to  $K_{\text{snaps}}^{\text{eff}} = (\sum_n W_n^2)^{-1}$  when the weights are normalized. This has the property that when the weights are equal,  $K_{\text{snaps}}^{\text{eff}} = K_{\text{snaps}}^{\text{tot}}$ , when all but one weight is negligible,  $K_{\text{snaps}}^{\text{eff}} \approx 1$ , and behaves appropriately for intermediate cases. Messerly et al.<sup>16</sup> propose a heuristic that MBAR estimates are sufficiently reliable to compute phase equilibria with ITIC when  $K_{\text{snaps}}^{\text{eff}} > 50$ . Section 3.3 tests whether this is a reasonable heuristic for GCMC-MBAR as well.

## 2.4 Basis functions

When applying GCMC-MBAR to different force field parameter sets ( $\theta_{\text{rr}} \neq \theta_{\text{ref}}$ ) it is necessary to recompute the internal energy for each snapshot ( $U(\mathbf{x}_n, N_n; \theta_{\text{rr}})$  in Equation

13). GCMC-HR typically requires millions of snapshots for precise estimates of  $\rho_{\text{liq}}^{\text{sat}}$ ,  $\rho_{\text{vap}}^{\text{sat}}$ ,  $P_{\text{vap}}^{\text{sat}}$ , and  $\Delta H_v$  over a wide range of  $T^{\text{sat}}$ . The naive GCMC-MBAR approach when  $\theta_{\text{rr}} \neq \theta_{\text{ref}}$  is to store the molecular configurations ( $\mathbf{x}_n$ ) at each snapshot and then recompute  $U(\mathbf{x}_n, N_n; \theta_{\text{rr}})$ . Although this “rerun” process in GOMC is orders of magnitude faster than performing direct GCMC simulations with  $\theta_{\text{rr}}$ , the naive approach is memory intensive and computationally expensive. Fortunately, basis functions can greatly accelerate the energy recomputation step.<sup>16,46</sup> Section 3.4 utilizes basis functions to rapidly recompute the non-bonded energies for  $\theta_{\text{rr}} \neq \theta_{\text{ref}}$ .

Basis functions are applicable whenever the energy can be separated linearly with respect to the force field parameters. For example, the Mie  $\lambda$ -6 non-bonded energy is separated into a repulsive and attractive term that can be expressed as

$$u^{\text{nb}}(C_6, C_\lambda; r) = C_\lambda r^{-\lambda} - C_6 r^{-6} \quad (19)$$

where  $C_6$  and  $C_\lambda$  are proportional to  $\epsilon\sigma^6$  and  $\epsilon\sigma^\lambda$ , respectively. Therefore, the total non-bonded energy between all  $\alpha$  and  $\beta$  sites ( $U_{\alpha\beta}^{\text{nb}}$ ) is simply

$$U_{\alpha\beta}^{\text{nb}}(C_6, C_\lambda) = C_\lambda \sum_{i \neq j} r_{ij}^{-\lambda} - C_6 \sum_{i \neq j} r_{ij}^{-6} = C_\lambda \Psi_\lambda + C_6 \Psi_6 \quad (20)$$

where  $\Psi_\lambda (\equiv \sum_{i \neq j} r_{ij}^{-\lambda})$  is the repulsive basis function,  $\Psi_6 (\equiv \sum_{i \neq j} r_{ij}^{-6})$  is the attractive basis function and, for simplicity,  $\sum_{i \neq j}$  denotes a sum over all unique pairwise interactions. Note that, because  $C_\lambda$  depends on  $\lambda$ , a separate repulsive basis function is required for each value of  $\lambda$ . For this reason, we adopt the common practice of limiting  $\lambda$  to integer values.

With Equation 20, the total non-bonded internal energy for all interaction sites of all  $K_{\text{snaps}}^{\text{tot}}$  snapshots can be recomputed for any  $\epsilon$  and  $\sigma$  with linear algebra instead of com-

puting  $u^{\text{nb}}(\theta_{\text{rr}}; r_{ij})$  for each unique pairwise interaction. Storing  $\Psi_\lambda$  and  $\Psi_6$  for  $K_{\text{snaps}}^{\text{tot}}$  snapshots also greatly reduces the memory storage load compared to storing  $K_{\text{snaps}}^{\text{tot}}$  configurational snapshots (which must be full-precision for reliable “rerun” results).

Although it is preferable to output  $\Psi_\lambda$  and  $\Psi_6$  at runtime, including this capability would require significant modification of GOMC. Instead, we utilize the GOMC “rerun” feature to indirectly compute  $\Psi_\lambda$  and  $\Psi_6$  post-simulation. Specifically, we recompute  $U_{\alpha\beta}^{\text{nb}}$  for  $\sigma_{\text{rr}} \neq \sigma_{\text{ref}}$  with  $\lambda_{\text{rr}} = \lambda_{\text{ref}}$  and  $\epsilon_{\text{rr}} = \epsilon_{\text{ref}}$ , such that  $C_{6,\text{rr}} \neq C_{6,\text{ref}}$  and  $C_{\lambda,\text{rr}} \neq C_{\lambda,\text{ref}}$ . We then perform an additional “rerun” calculation for each value of  $\lambda_{\text{rr}} \neq \lambda_{\text{ref}}$ . Having completed these “reruns,” the configuration files are no longer needed. Finally, we solve a system of equations for  $\Psi_6$  and  $\Psi_\lambda$ .

For example, the Lennard-Jones 12-6 and Mie 16-6 basis functions ( $\Psi_6$ ,  $\Psi_{12}$ , and  $\Psi_{16}$ ) are obtained by solving the following expression:

$$\begin{bmatrix} C_6(\sigma_{\text{ref}}, \epsilon_{\text{ref}}) & C_{12}(\sigma_{\text{ref}}, \epsilon_{\text{ref}}) & 0 \\ C_6(\sigma_{\text{rr}}, \epsilon_{\text{ref}}) & C_{12}(\sigma_{\text{rr}}, \epsilon_{\text{ref}}) & 0 \\ C_6(\sigma_{\text{rr}}, \epsilon_{\text{ref}}) & 0 & C_{16}(\sigma_{\text{rr}}, \epsilon_{\text{ref}}) \end{bmatrix} \begin{bmatrix} \Psi_6 \\ \Psi_{12} \\ \Psi_{16} \end{bmatrix} = \begin{bmatrix} U_{\alpha\beta}^{\text{nb}}(\sigma_{\text{ref}}, \epsilon_{\text{ref}}, 12) \\ U_{\alpha\beta}^{\text{nb}}(\sigma_{\text{rr}}, \epsilon_{\text{ref}}, 12) \\ U_{\alpha\beta}^{\text{nb}}(\sigma_{\text{rr}}, \epsilon_{\text{ref}}, 16) \end{bmatrix}$$

where  $U_{\alpha\beta}^{\text{nb}}(\sigma_{\text{ref}}, \epsilon_{\text{ref}}, 12)$  is the reference non-bonded energy,  $U_{\alpha\beta}^{\text{nb}}(\sigma_{\text{rr}}, \epsilon_{\text{ref}}, 12)$  is the “rerun” non-bonded energy for  $\sigma_{\text{rr}} \neq \sigma_{\text{ref}}$ ,  $\epsilon_{\text{rr}} = \epsilon_{\text{ref}}$ , and  $\lambda_{\text{rr}} = \lambda_{\text{ref}} = 12$ , and  $U_{\alpha\beta}^{\text{nb}}(\sigma_{\text{rr}}, \epsilon_{\text{ref}}, 16)$  is the “rerun” non-bonded energy for  $\sigma_{\text{rr}} \neq \sigma_{\text{ref}}$ ,  $\epsilon_{\text{rr}} = \epsilon_{\text{ref}}$ , and  $\lambda_{\text{rr}} = 16$ .

## 2.5 $\epsilon$ -scaling

Recently, Weidler and Gross proposed an  $\epsilon$ -scaling approach for converting the Transferable Anisotropic Mie (TAMie)<sup>7</sup> parameters into individualized (compound-specific) parameters (iTAMie).<sup>48</sup> The philosophy for individualized parameters is that some compounds have sufficient reliable experimental data to refine the force field parameters for

a specific molecule. However, refitting all non-bonded parameters simultaneously would likely lead to an underspecified optimization. To avoid overfitting, Weidler and Gross optimize a single adjustable parameter ( $\psi$ ) that scales all the  $\epsilon$  values in a molecule according to

$$\epsilon_{ii}^{\text{ind}} = \psi \times \epsilon_{ii}^{\text{tran}} \quad (21)$$

where  $\epsilon_{ii}^{\text{ind}}$  is the individualized  $\epsilon$  value for united-atom  $ii$ ,  $\epsilon_{ii}^{\text{tran}}$  is the corresponding transferable  $\epsilon$  value, and  $\psi$  is a fixed value for a given compound.

GCMC-MBAR is ideally suited for this “ $\epsilon$ -scaling” approach for at least two reasons. First, MBAR is most reliable when extrapolating in  $\epsilon$  rather than  $\sigma$  and/or  $\lambda$ .<sup>16</sup> Second, because  $\epsilon_{\text{rr}} = \psi \times \epsilon_{\text{ref}}$  while  $\sigma_{\text{rr}} = \sigma_{\text{ref}}$  and  $\lambda_{\text{rr}} = \lambda_{\text{ref}}$ , recomputing the total non-bonded energy for each snapshot is simply

$$U_{\text{rr}}^{\text{nb,tot}} = \psi \times U_{\text{ref}}^{\text{nb,tot}} \quad (22)$$

where  $U_{\text{rr}}^{\text{nb,tot}}$  and  $U_{\text{ref}}^{\text{nb,tot}}$  are the total non-bonded energy with  $\theta_{\text{rr}}$  and  $\theta_{\text{ref}}$ , respectively. Therefore,  $\epsilon$ -scaling does not require storing and recomputing configurations or basis functions.

Section 3.2 applies the GCMC-MBAR  $\epsilon$ -scaling approach to convert the MiPPE-SL semi-transferable parameters into individualized parameters (iMiPPE) for 8 branched alkanes and 11 alkynes. For consistency with the original MiPPE-SL optimization, we use the same scoring function for the branched alkanes and alkynes as Mick et al.<sup>12</sup> and

Soroush Barhaghi et al.,<sup>13</sup> respectively

$$\begin{aligned}
S = \frac{1}{N_{\text{exp}}} & \left[ w_0 \sum_{j=0}^{N_{\text{exp}}} APD(\rho_{\text{liq}}^{\text{sat}}(T_j^{\text{sat}})) + w_1 \sum_{j=0}^{N_{\text{exp}}} APD(\rho_{\text{vap}}^{\text{sat}}(T_j^{\text{sat}})) \right. \\
& + w_2 \sum_{j=0}^{N_{\text{exp}}} APD(P_{\text{vap}}^{\text{sat}}(T_j^{\text{sat}})) + w_3 \sum_{j=0}^{N_{\text{exp}}} APD(\Delta H_{\text{v}}(T_j^{\text{sat}})) \\
& + w_4 \sum_{j=0}^{N_{\text{exp}}-1} \frac{dAPD(\rho_{\text{liq}}^{\text{sat}}(T_j^{\text{sat}}))}{dT} + w_5 \sum_{j=0}^{N_{\text{exp}}-1} \frac{dAPD(\rho_{\text{vap}}^{\text{sat}}(T_j^{\text{sat}}))}{dT} \\
& \left. + w_6 \sum_{j=0}^{N_{\text{exp}}-1} \frac{dAPD(P_{\text{vap}}^{\text{sat}}(T_j^{\text{sat}}))}{dT} + w_7 \sum_{j=0}^{N_{\text{exp}}-1} \frac{dAPD(\Delta H_{\text{v}}(T_j^{\text{sat}}))}{dT} \right] \quad (23)
\end{aligned}$$

where  $S$  is the scoring function,  $N_{\text{exp}}$  is the number of (pseudo-)experimental data points,  $w_x$  are the weights for property  $x$  (see below),  $T_j^{\text{sat}}$  are the saturation temperatures for data point  $j$ , and the absolute percent deviation ( $APD$ ) is defined as

$$APD(X) = \left| \frac{X_{\text{sim}} - X_{\text{exp}}}{X_{\text{exp}}} \right| \times 100 \quad (24)$$

where  $X_{\text{sim}}$  and  $X_{\text{exp}}$  correspond to the respective simulation and (pseudo-) experimental values for property  $X$  (e.g.,  $\rho_{\text{liq}}^{\text{sat}}$ ). The derivative terms in Equation 23 are computed with

$$\frac{dAPD(X(T_j^{\text{sat}}))}{dT} = \frac{APD(X(T_{j+1}^{\text{sat}})) - APD(X(T_j^{\text{sat}}))}{T_{j+1}^{\text{sat}} - T_j^{\text{sat}}} \quad (25)$$

where  $j+1$  and  $j$  are sequential data points ordered according to  $T^{\text{sat}}$  and  $T_{j+1}^{\text{sat}} - T_j^{\text{sat}} = 10$  K.

In accordance with the work of Mick et al.<sup>12</sup> and Soroush Barhaghi et al.,<sup>13</sup> the target values ( $X_{\text{exp}}$ ) are not experimental data, rather they are computed values from correlations fit to experimental data. Specifically, the alkyne correlations are from the Design Institute for Physical Properties (DIPPR)<sup>49</sup> while the branched alkane correlations are from

the National Institute of Standards and Technology (NIST) Reference Fluid Properties (REFPROP) database.<sup>50–53</sup> Although REFPROP correlations exist for ethyne,<sup>53</sup> propyne,<sup>53</sup> and 1-butyne,<sup>54</sup> we utilize the DIPPR correlations for consistency within the alkyne family and to be consistent with Soroush Barhaghi et al.

We use the same weights ( $w_x$ ) in Equation 23 as Mick et al.<sup>12</sup> and Soroush Barhaghi et al.,<sup>13</sup> namely,  $w_x = (0.6135, 0.0123, 0.2455, 0.0245, 0.0613, 0.0061, 0.0245, 0.0123)$  and  $(0.757, 0, 0.152, 0, 0.076, 0, 0.015, 0)$  for branched alkanes and alkynes, respectively. The  $\rho_{\text{liq}}^{\text{sat}}$  weights are greatest due to both the high precision of experimental data and the high importance that the MiPPE force field reproduce this property. The  $P_{\text{vap}}^{\text{sat}}$  weights are second greatest, demonstrating the importance of this property but the slightly higher experimental uncertainties. The  $\rho_{\text{vap}}^{\text{sat}}$  and  $\Delta H_v$  weights are 0 for alkynes as the DIPPR database does not report  $\rho_{\text{vap}}^{\text{sat}}$  and the DIPPR  $\Delta H_v$  uncertainties are relatively large for most alkynes. Despite having weights that are an order of magnitude smaller, the derivative terms help ensure that the optimal force field has similar accuracy over the entire temperature range.

### 3 Results

Four different applications for GCMC-MBAR are demonstrated in this study, where slightly different types of simulation output are required. Section 3.1 demonstrates that GCMC-MBAR yields consistent results to those previously reported using histogram reweighting when the force field parameters do not change, i.e.,  $\theta_{\text{rr}} = \theta_{\text{ref}}$ . The same simulation output as GCMC-HR is used in this application, namely, a  $2 \times K_{\text{snaps}}^{\text{tot}}$  array containing the number of molecules ( $N$ ) and the internal energy ( $U$ ) for all  $K_{\text{snaps}}^{\text{tot}}$  snapshots. Section 3.2 demonstrates how these same data can be used with MBAR to perform a one-dimensional optimization with  $\epsilon$ -scaling. Section 3.3 investigates how well GCMC-MBAR

performs when predicting vapor-liquid coexistence properties for force field  $j$  from configurations sampled with force field  $i$ , where  $i$  and  $j$  are common force fields from the literature. In this case, a  $3 \times K_{\text{snaps}}^{\text{tot}}$  array is required, where the additional column is the internal energy computed with force field  $j$ . Section 3.4 presents a case study for optimizing Mie  $\lambda$ -6 non-bonded parameters for cyclohexane. Basis functions are employed as a computationally efficient method for predicting vapor-liquid phase equilibria with hundreds of  $\epsilon_{\text{CH}_2}$ ,  $\sigma_{\text{CH}_2}$ , and  $\lambda_{\text{CH}_2}$  values that are unknown at runtime. Using basis functions requires storing a  $(N_{\Psi} + 1) \times K_{\text{snaps}}^{\text{tot}}$  array, where  $N_{\Psi}$  is the number of basis functions and the  $N_{\Psi} + 1$  column corresponds to the values of  $N$ . For example, the Mie 16-6 potential has two basis functions ( $N_{\Psi} = 2$ ), one for  $\Psi_6$  and one for  $\Psi_{16}$ . Supporting Information contains basis function files for the TraPPE and MiPPE simulations of cyclohexane.

### 3.1 Validation of GCMC-MBAR for $\theta_{\text{rr}} = \theta_{\text{ref}}$

Section 2.3 demonstrated that MBAR and HR are mathematically equivalent in the limit of zero bin width when  $\theta_{\text{rr}} = \theta_{\text{ref}}$ . Figure 1 provides numerical validation that GCMC-MBAR and GCMC-HR yield indistinguishable vapor-liquid coexistence properties (tabulated GCMC-MBAR estimates and uncertainties are provided in Section S8 of Supporting Information). The evidence for this conclusion is that the median percent deviation is approximately zero and the largest deviations are within a few percent, which are typically smaller than the combined statistical uncertainties between HR and MBAR. Note that the uncertainties are largest near the critical point, i.e., reduced temperatures  $(T_r) \approx 1$ .

The percent deviations shown in Figure 1 are averaged over the 31 branched alkanes studied by Mick et al.<sup>12</sup> (only the MiPPE-SL data are re-evaluated) and the 11 alkynes studied by Soroush Barhaghi et al.<sup>13</sup> The GCMC-HR values used in Figure 1 were not recomputed in this study but were taken from the literature.<sup>12,13</sup> For a fair comparison



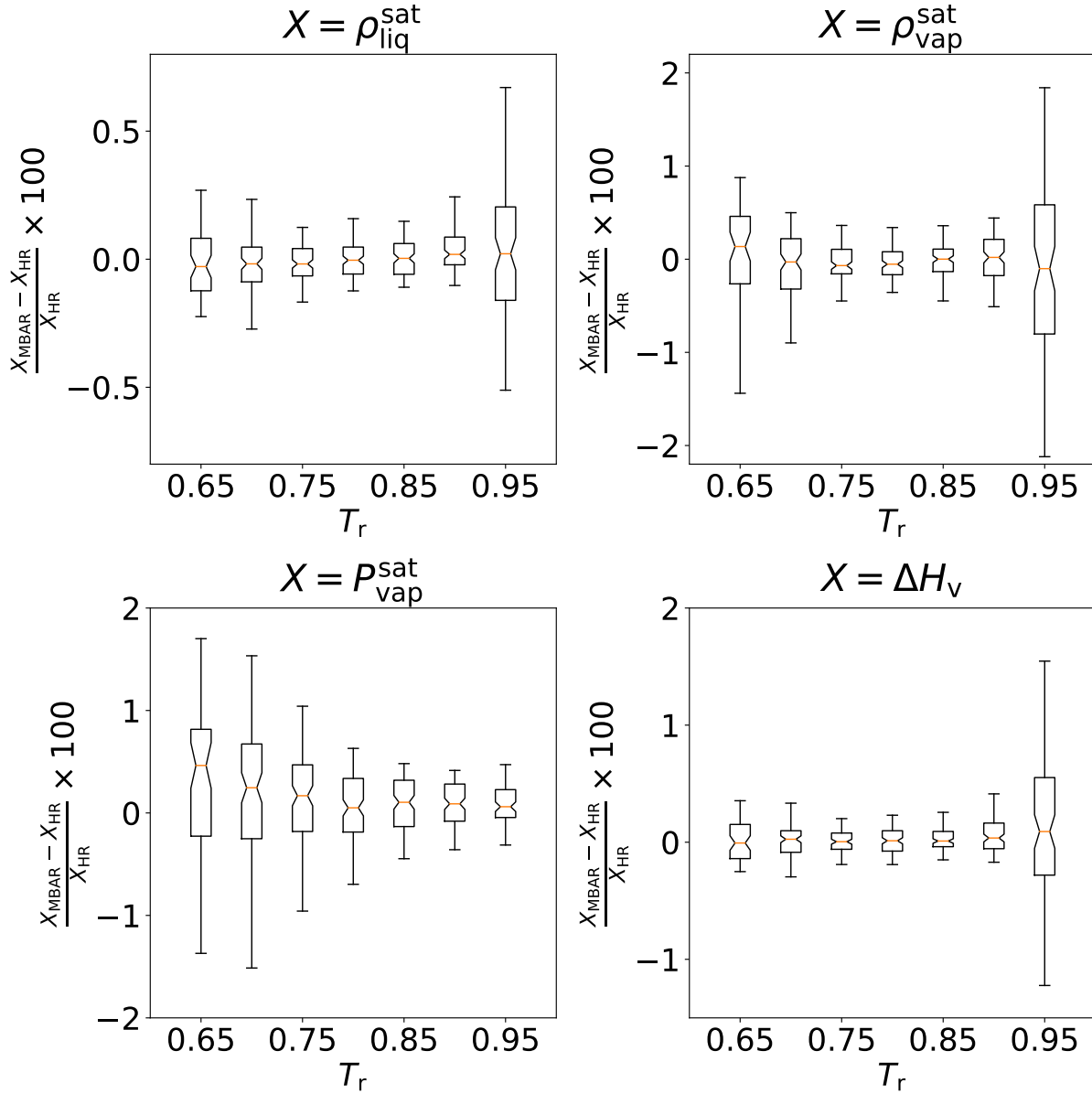


Figure 1: Percent deviations between coexistence properties computed using histogram reweighting (HR) and Multistate Bennett Acceptance Ratio (MBAR). The HR and MBAR results are in good agreement, i.e., within a few percent and a median percent deviation of approximately 0%. Top-left, top-right, bottom-left, and bottom-right panels correspond to saturated liquid density, saturated vapor density, saturated vapor pressure, and enthalpy of vaporization, respectively. Middle line denotes the median deviation, boxes depict the first and third quartiles, and whiskers represent the range that contains 95% of the data.

between GCMC-HR and GCMC-MBAR, the GCMC-MBAR values were computed using the same raw simulation data as Mick et al. and Soroush Barhaghi et al. However, for simplicity, we only reprocess one of the five replicate simulations.

### 3.2 Post-simulation $\epsilon$ -scaling with GCMC-MBAR

As discussed in Section 2.5,  $\epsilon$ -scaling is used to obtain an individualized (compound-specific) parameter ( $\psi$ ) for well-studied compounds, i.e., those with a large amount of reliable experimental data.<sup>48</sup> In this section, we demonstrate that GCMC-MBAR is an efficient tool for performing  $\epsilon$ -scaling.

Figure 2 presents the  $\epsilon$ -scaling results for 8 branched alkanes and 11 alkynes using the MiPPE-SL force field as  $\theta_{\text{ref}}$  ( $\psi = 1$ ). The same simulation data as discussed in Section 3.1 are re-purposed to compute phase equilibria properties over a range of  $\psi$  values (where  $\epsilon_{\text{rr}} = \psi \times \epsilon_{\text{ref}}$ ) without performing any additional simulations. Optimal  $\psi$  values for individualized MiPPE (iMiPPE) are provided in Section S5 of Supporting Information.

Weidler et al. tend to characterize the individualization as being useful when the scaling is greater than 0.4% (i.e.,  $|1 - \psi| > 0.004$ ).<sup>48</sup> With this rationale, 3-methylpentane is the only branched alkane that merits  $\epsilon$ -scaling with the MiPPE-SL force field. Similarly, the TAMie force field also found  $\psi \approx 1$  for all branched alkanes, except 3-methylpentane.

Figure 2 shows that the MiPPE parameters require a greater degree of scaling for alkynes than for branched alkanes. A truly transferable force field should have  $\psi \approx 1$  for all compounds. Although  $\psi$  values for iTAMie were not reported for alkynes, the largest  $\psi$  value for olefins, ethers, and ketones was  $\approx 1.01$ .<sup>48</sup> Therefore, the transferability of the MiPPE force field appears to be slightly poorer for 2-pentyne and 2-hexyne, which have an optimized  $\psi > 1.01$ .

It is also interesting that only 3 out of 19 compounds require  $\psi < 1$ . Thus, the well-depths appear to be slightly underestimated by the MiPPE force field. By contrast, this

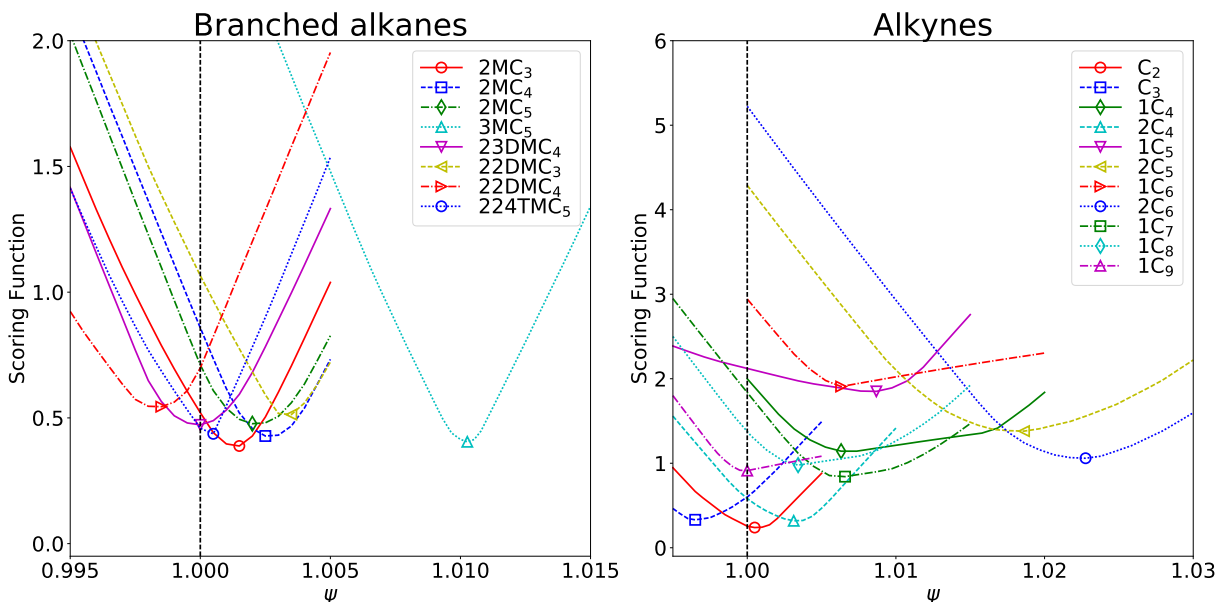


Figure 2: One-dimensional post-simulation optimization of  $\epsilon$ -scaling parameter ( $\psi$ ) for select branched alkanes (left) and alkynes (right) with MiPPE-SL as initial force field. MBAR enables prediction of scoring function over range of  $\psi$  values from configurations that were sampled with  $\psi = 1$  (dashed line). Open symbols correspond to the optimal  $\psi$  value for a given compound.

trend was not observed in Reference 48 for TAMie. Also, note that branched alkanes have a pronounced minimum in  $S$  with respect to  $\psi$ , whereas the minimum is more gradual for the alkynes. We attribute this, in part, to the fact that the alkynes do not include  $\Delta H_v$  (a property that depends strongly on  $\epsilon$ ) in the scoring function, i.e.,  $w_4 = 0$  and  $w_7 = 0$ .

### 3.3 Performance of GCMC-MBAR when varying $\epsilon$ , $\sigma$ , and $\lambda$

A more demanding test of GCMC-MBAR than  $\epsilon$ -scaling is to vary several non-bonded parameters simultaneously, including  $\sigma$  and  $\lambda$ . To perform a test of GCMC-MBAR when  $\theta_{\text{tr}} \not\approx \theta_{\text{ref}}$ , we estimate the phase equilibria of several branched alkanes for force field  $j$  by reweighting configurations sampled with force field  $i$  (denoted as  $\theta_i \Rightarrow \theta_j$ ), where  $i$  and  $j$  are either the MiPPE-gen, MiPPE-SL, TraPPE, or NERD force fields.

TraPPE  $\Leftrightarrow$  MiPPE-gen is the most challenging test as all three non-bonded parameters

( $\epsilon$ ,  $\sigma$ , and  $\lambda$ ) for all four united-atom types ( $\text{CH}_3$ ,  $\text{CH}_2$ ,  $\text{CH}$ , and  $\text{C}$ ) are different between the TraPPE and MiPPE-gen force fields. TraPPE  $\Rightarrow$  NERD is the second most challenging test because all  $\epsilon$  and  $\sigma$  values are substantially different but  $\lambda = 12$  for both force fields. MiPPE-gen  $\Rightarrow$  MiPPE-SL is considerably easier because these two force fields only differ in the  $\epsilon$  and/or  $\sigma$  values for the  $\text{CH}$  and  $\text{C}$  sites. Furthermore, the difference in  $\epsilon$  and  $\sigma$  values between MiPPE-gen and MiPPE-SL is significantly smaller than that between TraPPE and NERD (see Table 1). Therefore, MiPPE-gen  $\Rightarrow$  MiPPE-SL corresponds to  $\theta_{\text{tr}} \approx \theta_{\text{ref}}$ , which is an important scenario when fine-tuning force field parameters.

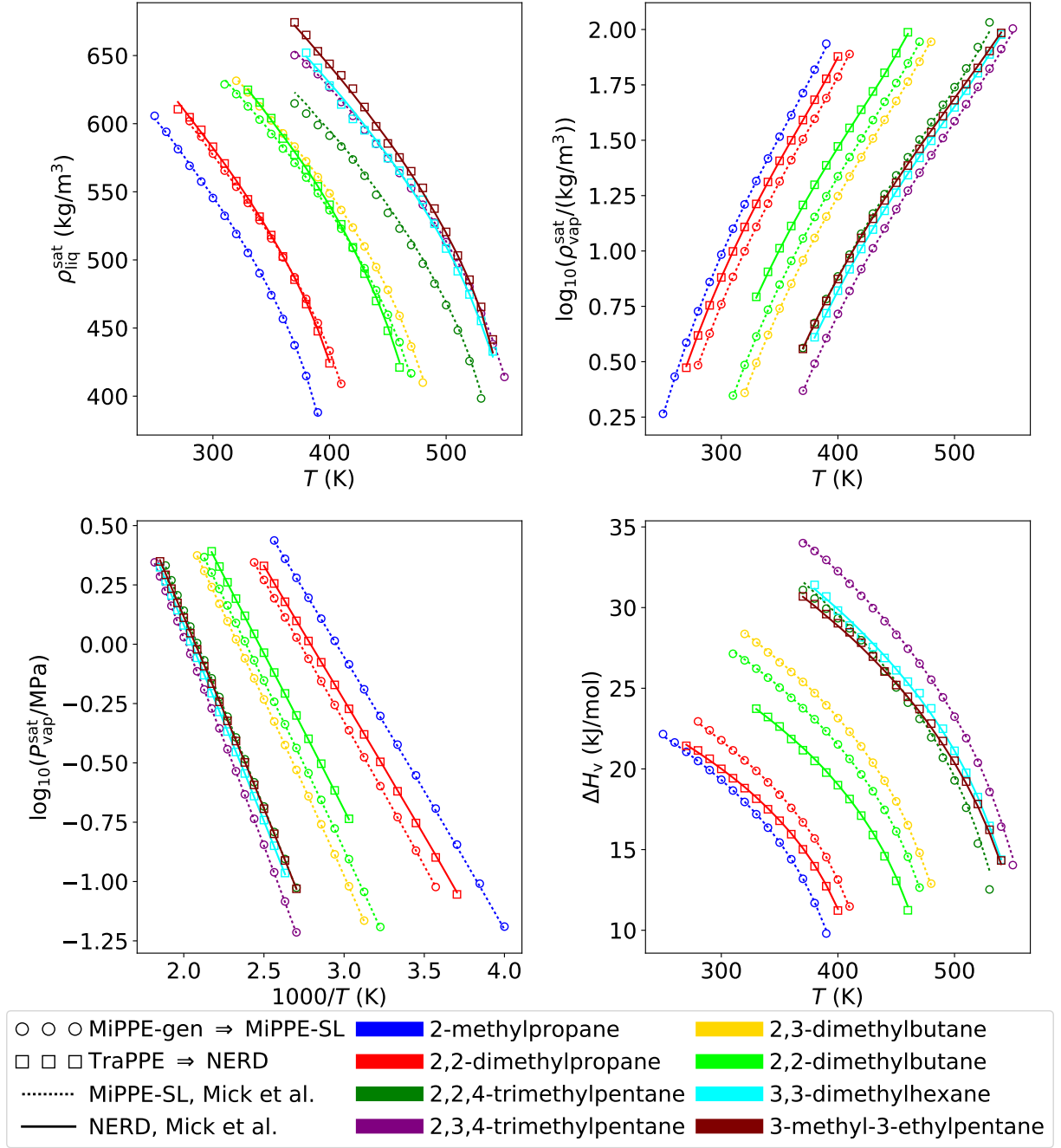


Figure 3: Comparison between GCMC-MBAR estimates (symbols,  $\theta_{rr} \neq \theta_{ref}$ ) and MBAR-HR literature values<sup>12</sup> (lines,  $\lambda_{rr} = \lambda_{ref}$ ). MBAR predicts both liquid and vapor properties accurately for  $\lambda_{rr} = \lambda_{ref}$ . GCMC-MBAR estimates for the NERD and MiPPE-SL force fields are computed using configurations sampled from TraPPE and MiPPE-gen, respectively. Top-left, top-right, bottom-left, and bottom-right panels correspond to saturated liquid density, saturated vapor density, saturated vapor pressure, and enthalpy of vaporization, respectively.

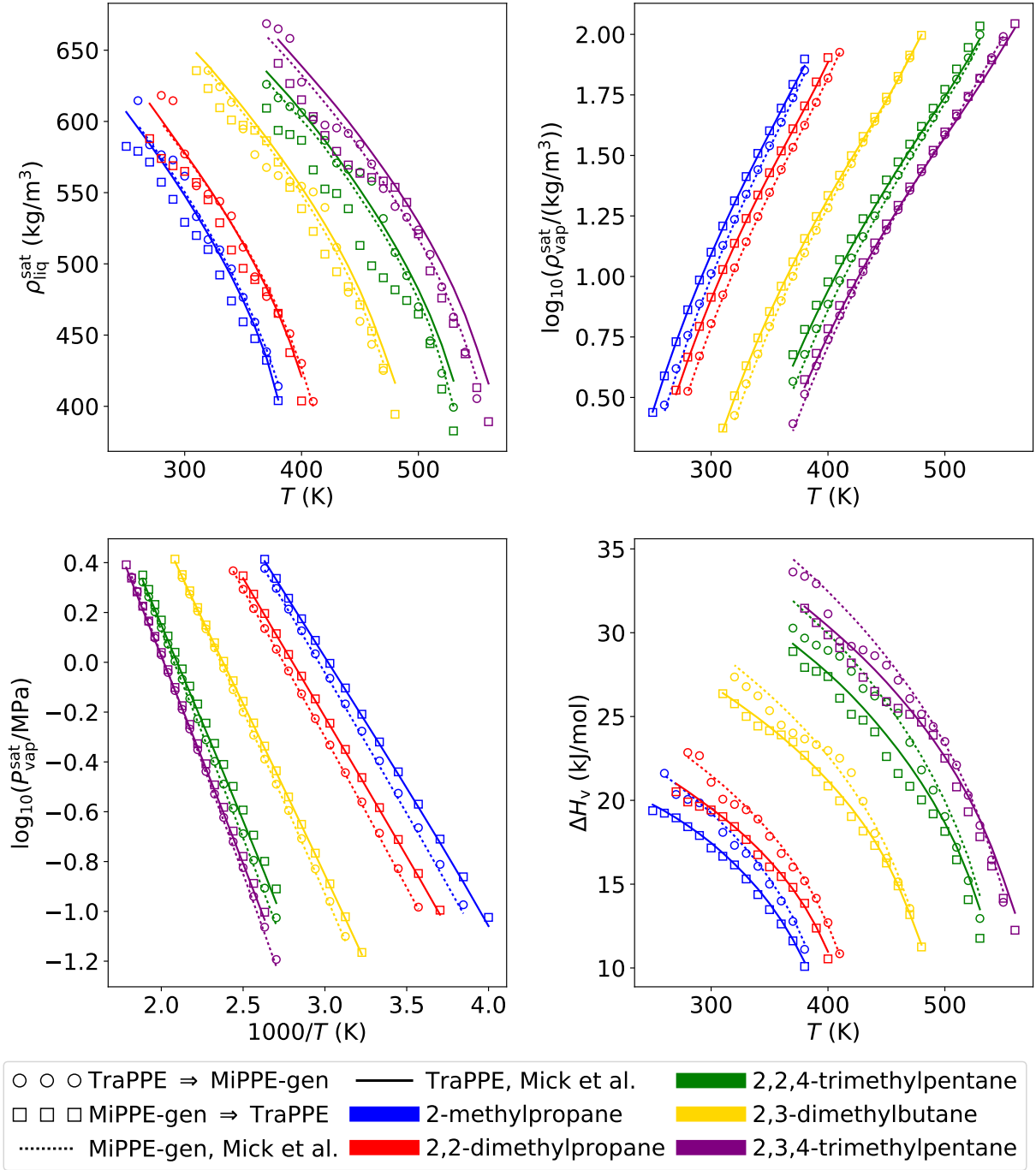


Figure 4: Comparison between GCMC-MBAR estimates (symbols,  $\theta_{rr} \neq \theta_{ref}$ ) and MBAR-HR literature values<sup>12</sup> (lines) with a non-constant repulsive exponent, i.e.,  $\lambda_{rr} \neq \lambda_{ref}$ . MBAR predicts only vapor properties accurately for  $\lambda_{rr} \neq \lambda_{ref}$ . GCMC-MBAR estimates for the TraPPE force field are computed using configurations sampled from MiPPE-gen, and vice versa. Top-left, top-right, bottom-left, and bottom-right panels correspond to saturated liquid density, saturated vapor density, saturated vapor pressure, and enthalpy of vaporization, respectively.

Figures 3 and 4 compare the GCMC-MBAR predicted values for  $\theta_{\text{rr}} \neq \theta_{\text{ref}}$  (symbols) to the literature GCMC-HR values (lines) obtained by direct simulation. Figure 3 contains  $\lambda_{\text{rr}} = \lambda_{\text{ref}}$  (TraPPE  $\Rightarrow$  NERD and MiPPE-gen  $\Rightarrow$  MiPPE-SL) while Figure 4 corresponds to  $\lambda_{\text{rr}} \neq \lambda_{\text{ref}}$  (TraPPE  $\Leftrightarrow$  MiPPE-gen).

The good agreement between corresponding symbols and lines in Figures 3 and 4 shows that MBAR is extremely reliable at predicting vapor phase properties ( $\rho_{\text{vap}}^{\text{sat}}$  and  $P_{\text{vap}}^{\text{sat}}$ ) for both  $\lambda_{\text{rr}} = \lambda_{\text{ref}}$  and  $\lambda_{\text{rr}} \neq \lambda_{\text{ref}}$ . Figure 3 demonstrates that GCMC-MBAR is remarkably accurate at predicting liquid phase properties ( $\rho_{\text{liq}}^{\text{sat}}$  and  $\Delta H_v$ , which depends on both phases) when  $\lambda_{\text{rr}} = \lambda_{\text{ref}}$ , even for the fairly significant differences in the TraPPE and NERD  $\sigma$  values. However, Figure 4 shows that GCMC-MBAR is unreliable for liquid phase properties when  $\lambda_{\text{rr}} \neq \lambda_{\text{ref}}$ . This undesirable behavior can be explained by the low number of effective snapshots in the liquid phase.

Figure 5 demonstrates that  $K_{\text{snaps}}^{\text{eff}}$  is typically much greater in the vapor phase ( $K_{\text{snaps}}^{\text{eff,vap}}$ ) than in the liquid phase ( $K_{\text{snaps}}^{\text{eff,liq}}$ ). Specifically,  $K_{\text{snaps}}^{\text{eff,vap}} \gg 50$ , while  $K_{\text{snaps}}^{\text{eff,liq}} < 50$  when  $\lambda_{\text{rr}} \neq \lambda_{\text{ref}}$  (TraPPE  $\Leftrightarrow$  MiPPE-gen) and  $K_{\text{snaps}}^{\text{eff,liq}} > 50$  for  $\lambda_{\text{rr}} = \lambda_{\text{ref}}$  (MiPPE-gen  $\Rightarrow$  MiPPE-SL and TraPPE  $\Rightarrow$  NERD). Therefore, similar to the conclusions of Messerly et al.<sup>16</sup> for MBAR-ITIC,  $K_{\text{snaps}}^{\text{eff}} > 50$  is a good indication that the GCMC-MBAR estimates are reliable. In comparison, MBAR-ITIC experiences even worse overlap at near-saturated liquid conditions ( $\bar{K}_{\text{snaps,liq}}^{\text{eff}} \approx 1$ ) for TraPPE  $\Rightarrow$  MiPPE-gen ( $\lambda_{\text{rr}} \neq \lambda_{\text{ref}}$ ).<sup>16</sup>

The strong disparity between  $K_{\text{snaps}}^{\text{eff,vap}}$  and  $K_{\text{snaps}}^{\text{eff,liq}}$  when  $\lambda_{\text{rr}} \neq \lambda_{\text{ref}}$  is expected for at least two reasons. The first reason is that the vapor phase has fewer molecules overall.  $K_{\text{snaps}}^{\text{eff}}$  (or alternatively  $W_n$ ) is greatest when the reduced potential energy ( $u$  in Equation 13) is similar for  $\theta_{\text{rr}}$  and  $\theta_{\text{ref}}$ , such that the ratio of Boltzmann factors is close to unity. The reduced potential energy is proportional to the total internal energy ( $U$ ), which is an extensive property that depends on both  $N$  and  $\theta$ . Therefore, even when  $\theta_{\text{rr}} \neq \theta_{\text{ref}}$ , small values of  $N$  lead to  $u(\theta_{\text{rr}}) \approx u(\theta_{\text{ref}})$ .

The second reason is that there are more instances of close-range interactions in the liquid phase. Varying  $\lambda$  changes the slope and location of the repulsive wall, which greatly impacts the non-bonded energy at short distances (i.e.,  $r < \sigma$ ). These large changes in  $U$  when  $\lambda_{rr} \neq \lambda_{ref}$  cause  $W_n \approx 0$  for the majority of liquid phase configurations. For similar reasons, the overlap in the liquid phase is markedly worse when  $\sigma_{rr} \neq \sigma_{ref}$ . For example,  $K_{snaps}^{eff,liq}$  is significantly greater for MiPPE-gen  $\Rightarrow$  MiPPE-SL than TraPPE  $\Rightarrow$  NERD (see Figure 5).

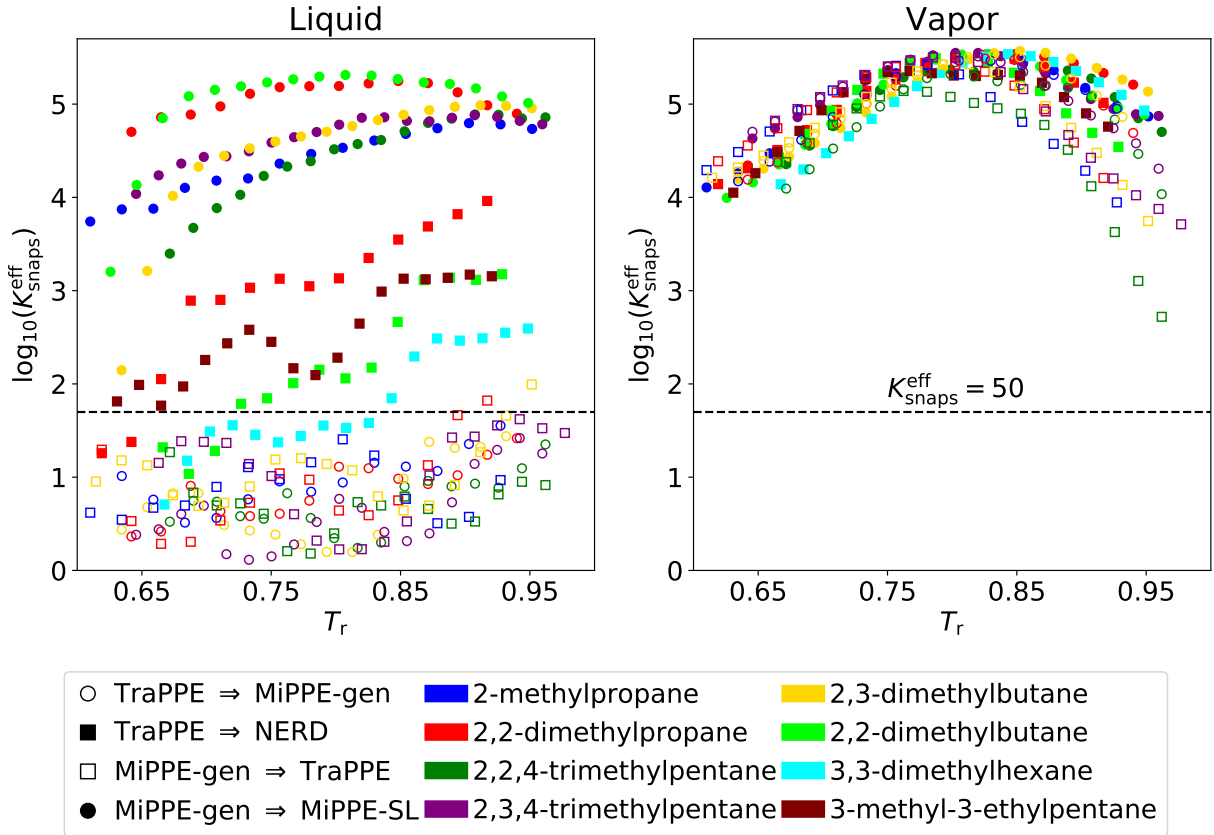


Figure 5: Number of effective snapshots ( $K_{snaps}^{eff}$ ) in the liquid (left panel) and vapor (right panel) phases. Good overlap ( $K_{snaps}^{eff} \gg 50$ ) is achieved in the vapor phase for each system while poor overlap in liquid phase ( $K_{snaps}^{eff} < 50$ ) is observed for  $\lambda_{rr} \neq \lambda_{ref}$ . The amount of overlap explains why GCMC-MBAR is highly reliable in both phases for  $\lambda_{rr} = \lambda_{ref}$  (see Figure 3), while GCMC-MBAR is not reliable in the liquid phase for  $\lambda_{rr} \neq \lambda_{ref}$  (see Figure 4). Color scheme is the same as Figures 3 and 4. Closed and open symbols correspond to  $\lambda_{rr} = \lambda_{ref}$  and  $\lambda_{rr} \neq \lambda_{ref}$ , respectively.



Although GCMC-MBAR is unreliable for  $\rho_{\text{liq}}^{\text{sat}}$  and  $\Delta H_v$  when  $\lambda_{\text{rr}} \neq \lambda_{\text{ref}}$ , GCMC-MBAR provides considerable improvement in predicting  $\rho_{\text{vap}}^{\text{sat}}$  and  $P_{\text{vap}}^{\text{sat}}$  when  $\lambda_{\text{rr}} \neq \lambda_{\text{ref}}$  compared to what was previously observed for MBAR-ITIC.<sup>16</sup> Therefore, similar to MBAR-ITIC, optimizing Mie  $\lambda$ -6 parameters requires performing direct simulations for each value of  $\lambda$ . However, as opposed to MBAR-ITIC, GCMC-MBAR can help determine where these additional simulations should be performed, i.e., GCMC-MBAR can localize the likely optimal  $\epsilon$  and  $\sigma$  values for  $\lambda_{\text{rr}} \neq \lambda_{\text{ref}}$ .

We recommend the following algorithm for optimizing Mie  $\lambda$ -6 parameters with GCMC-MBAR:

1. Simulate initial reference force field ( $\theta_{\text{ref}}^{(0)}$ ), e.g., TraPPE
2. Compute basis functions for various values of  $\lambda$
3. Optimize  $\epsilon$  and  $\sigma$  for each  $\lambda$  ( $\epsilon^{(i)}, \sigma^{(i)}$ ) by:
  - (a) Estimating  $\rho_{\text{liq}}^{\text{sat}}, \rho_{\text{vap}}^{\text{sat}}, P_{\text{vap}}^{\text{sat}}$ , and  $\Delta H_v$  with GCMC-MBAR
  - (b) Minimizing scoring function ( $S$ )
4. Perform additional simulations with  $\epsilon^{(i)}, \sigma^{(i)}$  from Step 3 for each  $\lambda$
5. Repeat Steps 3 and 4 until  $\min(K_{\text{snaps}}^{\text{eff}}) \gg 50$  for  $\theta^{(i)}$
6. Determine overall optimal parameter set ( $\theta_{\text{opt}}$ )

The stopping criterion is based on the minimum number of effective snapshots  $\min(K_{\text{snaps}}^{\text{eff}})$ , which always corresponds to the liquid phase at lower values of  $T^{\text{sat}}$  (see Figure 5). Therefore, GCMC-MBAR estimates should be reliable over the entire range of saturation temperatures when  $\min(K_{\text{snaps}}^{\text{eff}}) \gg 50$ . If this is true for the optimal region of parameter space, any additional iterations would be ill-advised and unnecessary as the optimization would

primarily be fitting to the uncertainty in the simulation output. Section 3.4 presents an application of this approach for cyclohexane.

### 3.4 Case Study: Post-simulation optimization of cyclohexane Mie $\lambda$ -6 parameters

In this section, we present how GCMC-MBAR can rapidly convert a pre-tuned Lennard-Jones 12-6 potential (TraPPE) into a Mie  $\lambda$ -6 potential (MiPPE) without performing hundreds of simulations. We have chosen cyclohexane for this case study as MiPPE does not yet have non-bonded parameters for this compound, while the TraPPE force field does. Also, because cyclohexane consists of a single united-atom site type ( $\text{CH}_2$ ), it is a convenient molecule for representing the scoring function in 2-dimensions ( $\epsilon_{\text{CH}_2}$  and  $\sigma_{\text{CH}_2}$  for a given value of  $\lambda_{\text{CH}_2}$ ).

The scoring function is computed with the branched alkane weights ( $w_x$ ) and REFPROP correlations<sup>50,55</sup> as target data ( $X_{\text{exp}}$ ). To avoid finite size effects in the near critical region, data are excluded for  $T^{\text{sat}} > 0.95T_c$ . Specifically,  $X_{\text{exp}}$  consists of REFPROP  $\rho_{\text{liq}}^{\text{sat}}$ ,  $\rho_{\text{vap}}^{\text{sat}}$ ,  $P_{\text{vap}}^{\text{sat}}$ , and  $\Delta H_v$  values from 360 K to 520 K with 5 K intervals.

Figure 6 depicts the scoring function for the first iteration of the optimization, where GCMC simulations were performed with the TraPPE parameters (depicted as a white triangle in Figures 6 and 7). Similar figures have been reported in the literature using GCMC-HR.<sup>12,13</sup> The key difference is that the heat maps reported in the literature were obtained by performing GCMC simulations with hundreds of different parameter sets. By contrast, the results shown in Figure 6 were obtained by performing GCMC simulations with a single parameter set, namely, the TraPPE parameters. MBAR reweights these same configurations for all other parameter sets. Furthermore,  $U(\theta_{\text{tr}})$  is computed with basis functions, enabling the GCMC-MBAR recompute step to be extremely fast.

Note that the TraPPE force field utilizes a Lennard-Jones 12-6 potential (i.e.,  $\lambda_{\text{TraPPE}} = 12$ ) and, therefore, the results in the top-left panel of Figures 6 and 7 are for the case where  $\lambda_{\text{rr}} = \lambda_{\text{ref}} = 12$ , while the other panels correspond to  $\lambda_{\text{rr}} \neq \lambda_{\text{ref}}$ . Figure 7 shows that, as expected, the average number of effective snapshots in the liquid phase ( $\bar{K}_{\text{snaps,liq}}^{\text{eff}}$ ) is much greater for  $\lambda_{\text{rr}} = \lambda_{\text{ref}}$  than for  $\lambda_{\text{rr}} \neq \lambda_{\text{ref}}$ .

When  $\lambda_{\text{rr}} = \lambda_{\text{ref}}$ , MBAR-ITIC is reliable ( $\bar{K}_{\text{snaps,liq}}^{\text{eff}} > 50$ ) for  $\sigma_{\text{rr}} = \sigma_{\text{ref}} \pm 0.0025$  nm,<sup>16</sup> while Figure 7 (top left panel) suggests that GCMC-MBAR is reliable over a much wider range ( $\sigma_{\text{rr}} \approx \sigma_{\text{ref}} \pm 0.01$  nm). Although the overlap is significantly better for GCMC-MBAR compared to MBAR-ITIC for  $\lambda_{\text{rr}} \neq \lambda_{\text{ref}}$ , Figure 7 demonstrates that GCMC-MBAR and MBAR-ITIC follow a similar trend, namely, the high  $\bar{K}_{\text{snaps,liq}}^{\text{eff}}$  region corresponds to  $\sigma_{\text{rr}} < \sigma_{\text{ref}}$  when  $\lambda_{\text{rr}} > \lambda_{\text{ref}}$  and  $\epsilon_{\text{rr}} > \epsilon_{\text{ref}}$ . This poses a challenge for parameterization because the optimal  $\sigma_{\text{CH}_2}$  value is fairly constant while the optimal  $\epsilon_{\text{CH}_2}$  value tends to increase with respect to  $\lambda_{\text{CH}_2}$ .

In addition, the smooth contours in Figure 6 for  $\lambda_{\text{rr}} = \lambda_{\text{ref}} = 12$  and the wide range of parameters over which  $\bar{K}_{\text{snaps}}^{\text{eff,liq}} \gg 50$  suggests that GCMC-MBAR is highly reliable for optimizing  $\epsilon_{\text{CH}_2}$  and  $\sigma_{\text{CH}_2}$  for a fixed value of  $\lambda_{\text{CH}_2}$ . Even more remarkable, considering the erroneous prediction of  $\rho_{\text{liq}}^{\text{sat}}$  and  $\Delta H_{\text{v}}$  for  $\lambda_{\text{rr}} \neq \lambda_{\text{ref}}$  (see Figure 4), is that GCMC-MBAR predicts smooth contours for  $\lambda \neq 12$  despite lower values of  $\bar{K}_{\text{snaps}}^{\text{eff,liq}}$ . This characteristic would be important when implementing gradient descent optimization schemes. By contrast, MBAR-ITIC yields sporadic contours for  $\lambda_{\text{rr}} \neq \lambda_{\text{ref}}$  that are unreliable for optimization.<sup>16</sup>

The optimal parameter sets (depicted as white “X”s in Figures 6 and 7) correspond to the lowest value of  $S$  for each value of  $\lambda_{\text{CH}_2}$ . Having minimized the scoring function for  $\lambda_{\text{CH}_2} = 12, 14, 16, 18$ , and 20 (not shown in Figure 6), we perform additional simulations with the optimal parameter sets ( $\theta^{(1)}$ ) serving as new reference parameter sets. Because GCMC-MBAR is reliable over a wide range of  $\epsilon_{\text{CH}_2}$  and  $\sigma_{\text{CH}_2}$  values for  $\lambda_{\text{rr}} = \lambda_{\text{ref}}$ , we only

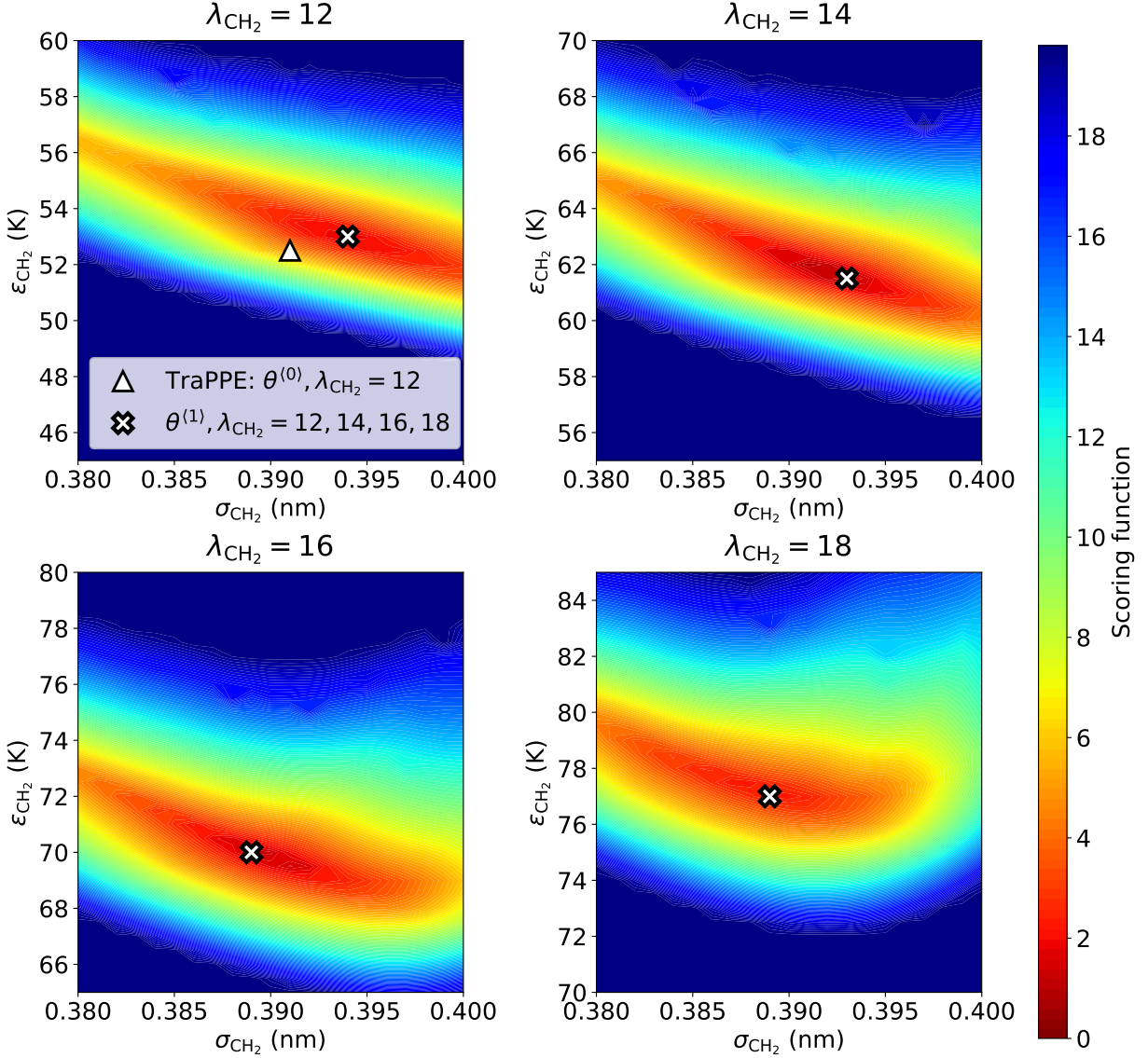


Figure 6: First iteration scoring function values with respect to  $\epsilon_{\text{CH}_2}$  and  $\sigma_{\text{CH}_2}$  for cyclohexane. GCMC-MBAR enables rapid optimization of Mie  $\lambda$ -6 parameters from a single reference force field ( $\theta_{\text{ref}}^{(0)} = \theta_{\text{TraPPE}}$ , depicted as a white triangle). Top-left, top-right, bottom-left, and bottom-right panels correspond  $\lambda_{\text{CH}_2} = 12$ ,  $\lambda_{\text{CH}_2} = 14$ ,  $\lambda_{\text{CH}_2} = 16$ ,  $\lambda_{\text{CH}_2} = 18$ , respectively. White “X”s represent the optimal parameter sets (the lowest value of  $S$ ) for each  $\lambda_{\text{CH}_2}$ .

reweight snapshots generated with the same value of  $\lambda_{\text{CH}_2}$ . Also, because the optimal  $\epsilon_{\text{CH}_2}$  and  $\sigma_{\text{CH}_2}$  parameters for  $\lambda_{\text{CH}_2} = 12$  already have  $\min(K_{\text{snaps}}^{\text{eff}}) \gg 50$ , we only consider  $\lambda_{\text{CH}_2} \geq 14$ .

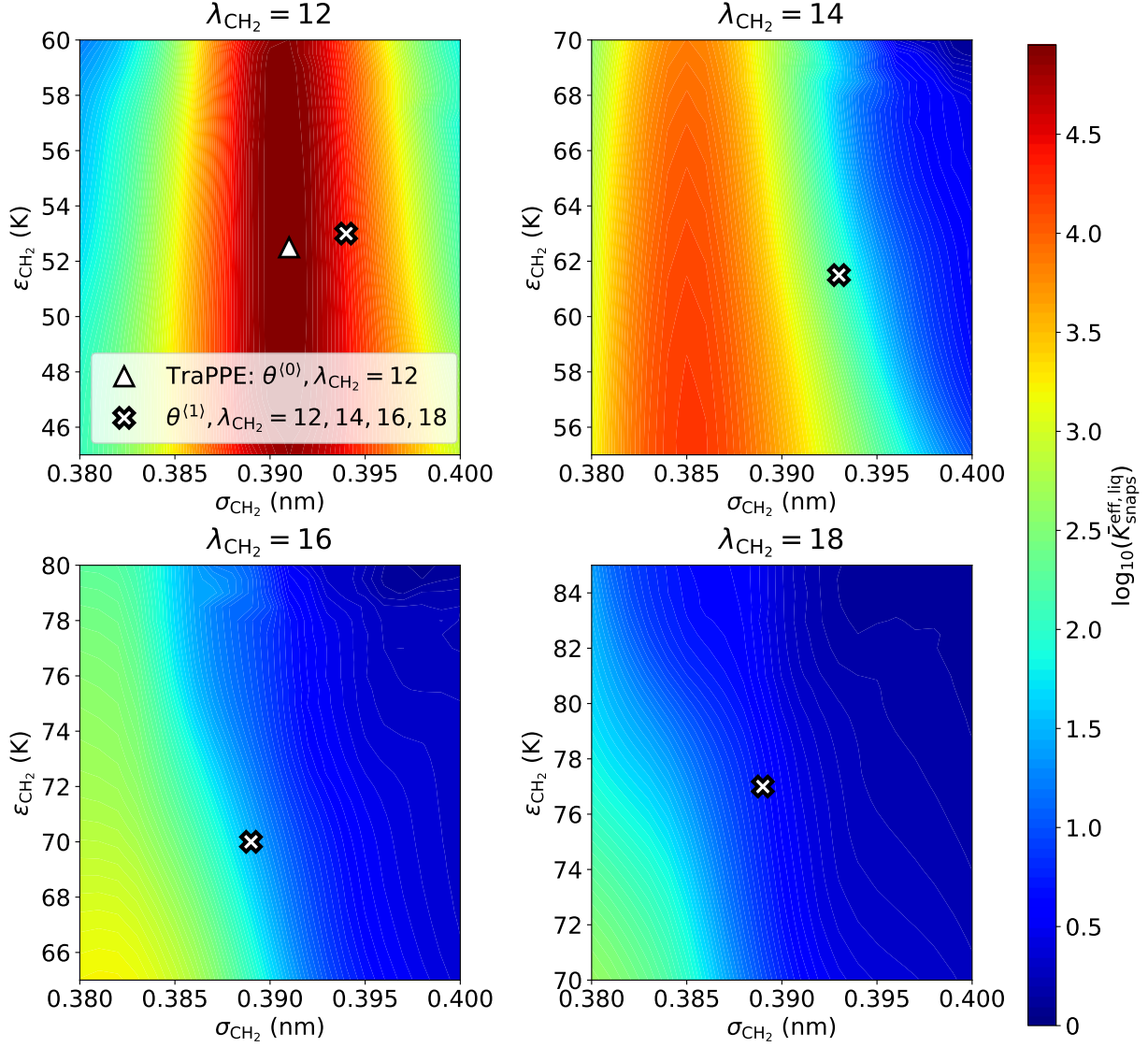


Figure 7: First iteration average number of effective snapshots in the liquid phase ( $\bar{K}_{\text{snaps}}^{\text{eff,liq}}$ ) with respect to  $\epsilon_{\text{CH}_2}$  and  $\sigma_{\text{CH}_2}$  for cyclohexane.  $\bar{K}_{\text{snaps}}^{\text{eff,liq}} \gg 50$  over a wide range of parameters when  $\lambda_{\text{rr}} = \lambda_{\text{ref}} = 12$  (top-left panel), while  $\bar{K}_{\text{snaps}}^{\text{eff,liq}}$  is typically less than 50 for  $\lambda_{\text{rr}} \neq \lambda_{\text{ref}}$  (other panels). Top-left, top-right, bottom-left, and bottom-right panels correspond  $\lambda_{\text{CH}_2} = 12$ ,  $\lambda_{\text{CH}_2} = 14$ ,  $\lambda_{\text{CH}_2} = 16$ ,  $\lambda_{\text{CH}_2} = 18$ , respectively. Symbols are the same as Figure 6.

Figure 8 presents the results from this second iteration of the two-dimensional optimization for each  $\lambda_{\text{CH}_2}$ . Also depicted in the  $\lambda_{\text{CH}_2} = 16$  panel are the TAMie cyclohexane parameters.<sup>56</sup> Note that the first iteration optimal parameter sets (white “X”s) are similar

to the second iteration (white “+”s and star), which provides further evidence that the first iteration results for  $\lambda_{\text{rr}} \neq \lambda_{\text{ref}}$  are quite reliable. We verify that the optimization has converged, i.e.,  $\min(K_{\text{snaps}}^{\text{eff}}) \gg 50$  for  $\theta_{\text{opt}}^{(2)}$  (see Figure S6 in Supporting Information).

Table 2: Optimal Mie  $\lambda$ -6 cyclohexane parameters for  $\lambda_{\text{CH}_2} = 12, 14, 16, 18,$  and  $20$ . Superscript denotes the iteration stage of the optimization. Stage 0 corresponds to the TraPPE force field and Stage 2 for  $\lambda_{\text{CH}_2} = 16$  is the MiPPE force field. Final column reports the optimal scoring function ( $S_{\text{opt}}$ ) for each  $\lambda_{\text{CH}_2}$  (computed with  $\theta^{(1)}$  for  $\lambda_{\text{CH}_2} = 12$  and with  $\theta^{(2)}$  for  $\lambda_{\text{CH}_2} = 14, 16, 18,$  and  $20$ ).

$\lambda_{\text{CH}_2}$	$\epsilon_{\text{CH}_2}^{(0)}/k_{\text{B}}$ (K)	$\sigma_{\text{CH}_2}^{(0)}$ (nm)	$\epsilon_{\text{CH}_2}^{(1)}/k_{\text{B}}$ (K)	$\sigma_{\text{CH}_2}^{(1)}$ (nm)	$\epsilon_{\text{CH}_2}^{(2)}/k_{\text{B}}$ (K)	$\sigma_{\text{CH}_2}^{(2)}$ (nm)	$S_{\text{opt}}$
12	52.5	0.391	53.0	0.394	–	–	1.79
14	–	–	61.5	0.393	61.5	0.393	1.03
16	–	–	70.0	0.389	69.7	0.3902	0.463
18	–	–	77.0	0.389	76.5	0.390	0.791
20	–	–	84.0	0.388	82.5	0.389	1.07

Table 2 summarizes the parameter sets obtained at each stage of the optimization. Table 2 shows that, similar to other alkanes in the MiPPE force field,  $\lambda_{\text{CH}_2} = 16$  is once again found to be the optimal repulsive exponent (with the lowest  $S$ ) when only considering even integer values. This optimal  $\lambda_{\text{CH}_2} = 16$  value also agrees with the TAMie force field. The overall optimal parameter set ( $\theta^{(2)}$ ,  $\lambda_{\text{CH}_2} = 16$ ) is included in Table 1 as the MiPPE cyclohexane parameters.  $\epsilon_{\text{CH}_2}$  and  $\sigma_{\text{CH}_2}$  are reported with three and four digits, respectively, consistent with other MiPPE parameters and to provide a qualitative measure of uncertainty. Note the close agreement between the MiPPE and TAMie parameters<sup>56</sup> ( $\epsilon_{\text{CH}_2}/k_{\text{B}} = 69.568$  K,  $\sigma_{\text{CH}_2} = 0.38967$  nm, and  $\lambda_{\text{CH}_2} = 16$ ), which were optimized with a slightly different objective function and experimental data set.

It is important to verify that the final parameter set does indeed provide accurate predictions of vapor-liquid coexistence properties. For this reason, after completing the optimization, we perform direct GCMC simulations with the overall optimal parameter set (MiPPE). Twenty independent replicate simulations are performed at each state point

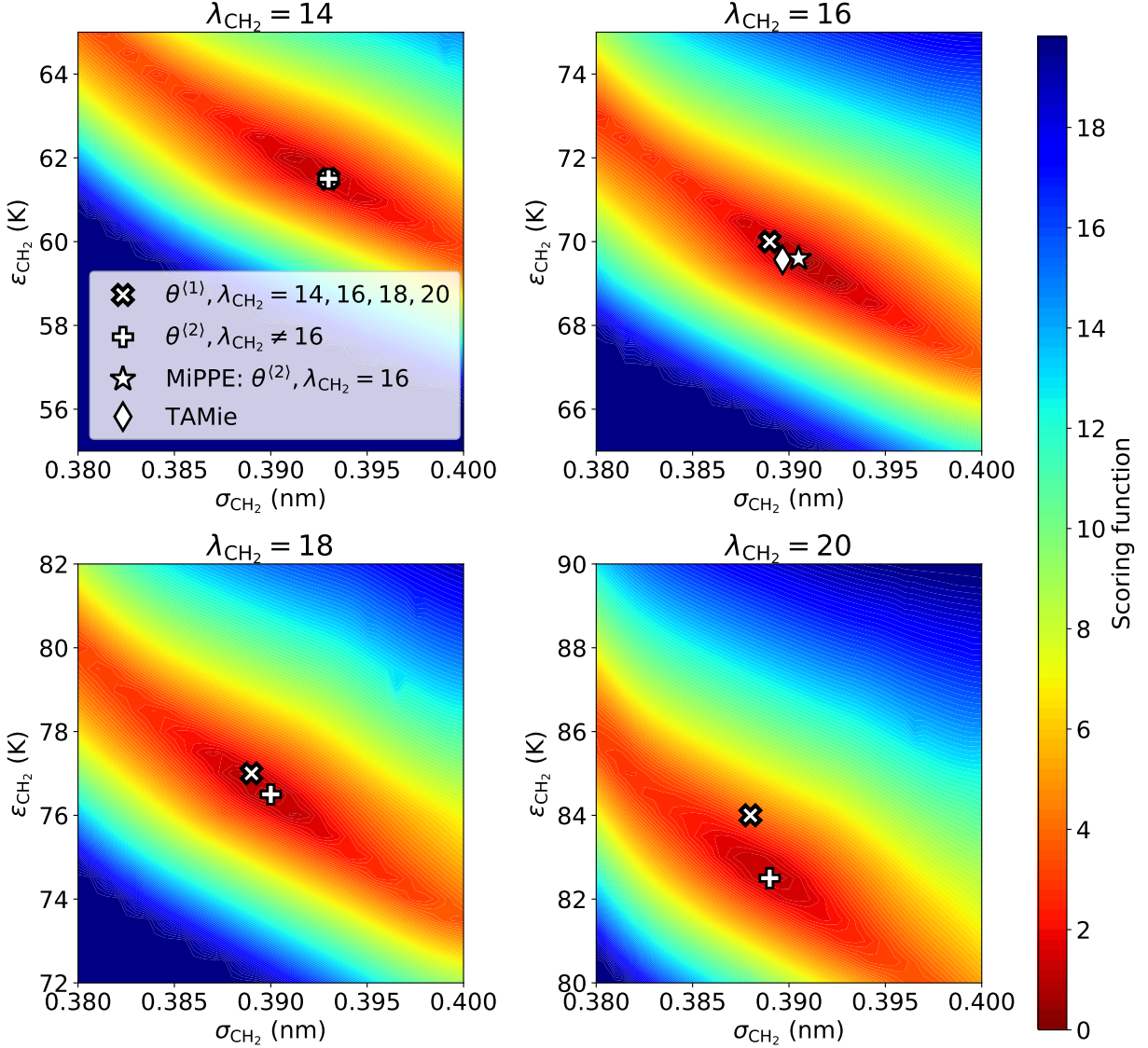


Figure 8: Second iteration scoring function values with respect to  $\epsilon_{\text{CH}_2}$  and  $\sigma_{\text{CH}_2}$  for cyclohexane. Pseudo-optimal parameter sets from first iteration serve as reliable reference parameter sets for refining the optimization. Top-left, top-right, bottom-left, and bottom-right panels correspond  $\lambda_{\text{CH}_2} = 14$ ,  $\lambda_{\text{CH}_2} = 16$ ,  $\lambda_{\text{CH}_2} = 18$ , and  $\lambda_{\text{CH}_2} = 20$ , respectively. White star represents the overall optimal parameter set (MiPPE:  $\theta^{(2)}$ ,  $\lambda_{\text{CH}_2} = 16$ ), white “+”s correspond to optimal parameter sets ( $\theta^{(2)}$ ) for  $\lambda_{\text{CH}_2} \neq 16$ , and the white diamond is the TAMie parameter set (for  $\lambda_{\text{CH}_2} = 16$ ). White “X”s depict the single reference force field for each  $\lambda_{\text{CH}_2}$  (i.e.,  $\lambda_{\text{rr}} = \lambda_{\text{ref}}$ ) and are the same as Figures 6 and 7.

$(\mu, V, T)$  to reduce and rigorously quantify the statistical uncertainties for the MiPPE cyclohexane results.



Furthermore, because we have performed the MiPPE parameterization with a relatively small box size (27 nm<sup>3</sup>), it is important to test for the existence of finite-size effects. By performing additional simulations with a larger box size (42.875 nm<sup>3</sup>), we conclude that finite-size effects are only significant (larger than the combined uncertainties) for  $\rho_{\text{vap}}^{\text{sat}}$  and  $\Delta H_{\text{v}}$  near the critical point. Specifically, we estimate that finite-size effects for both  $\rho_{\text{vap}}^{\text{sat}}$  and  $\Delta H_{\text{v}}$  are between 1% and 2% for  $T^{\text{sat}} > 480$  K (see Section S6.5 in Supporting Information).

Figure 9 is provided to quantify the improved accuracy achieved for the two iterations by comparing the percent deviations for between pseudo-experimental (REFPROP) values and the zeroth iteration (TraPPE:  $\theta^{(0)}$ ,  $\lambda_{\text{CH}_2} = 12$ ), first iteration ( $\theta^{(1)}$  for  $\lambda_{\text{CH}_2} = 14, 16$ , and 18), and final iteration (MiPPE:  $\theta^{(2)}$ ,  $\lambda_{\text{CH}_2} = 16$ ) parameter sets. Figure 9 also includes percent deviations for several of the most reliable force fields from the literature.<sup>22,24,27,56–59</sup> Additional phase equilibria and deviation plots are provided in Section S6 of Supporting Information, including a detailed comparison between the MiPPE and TAMie force fields.



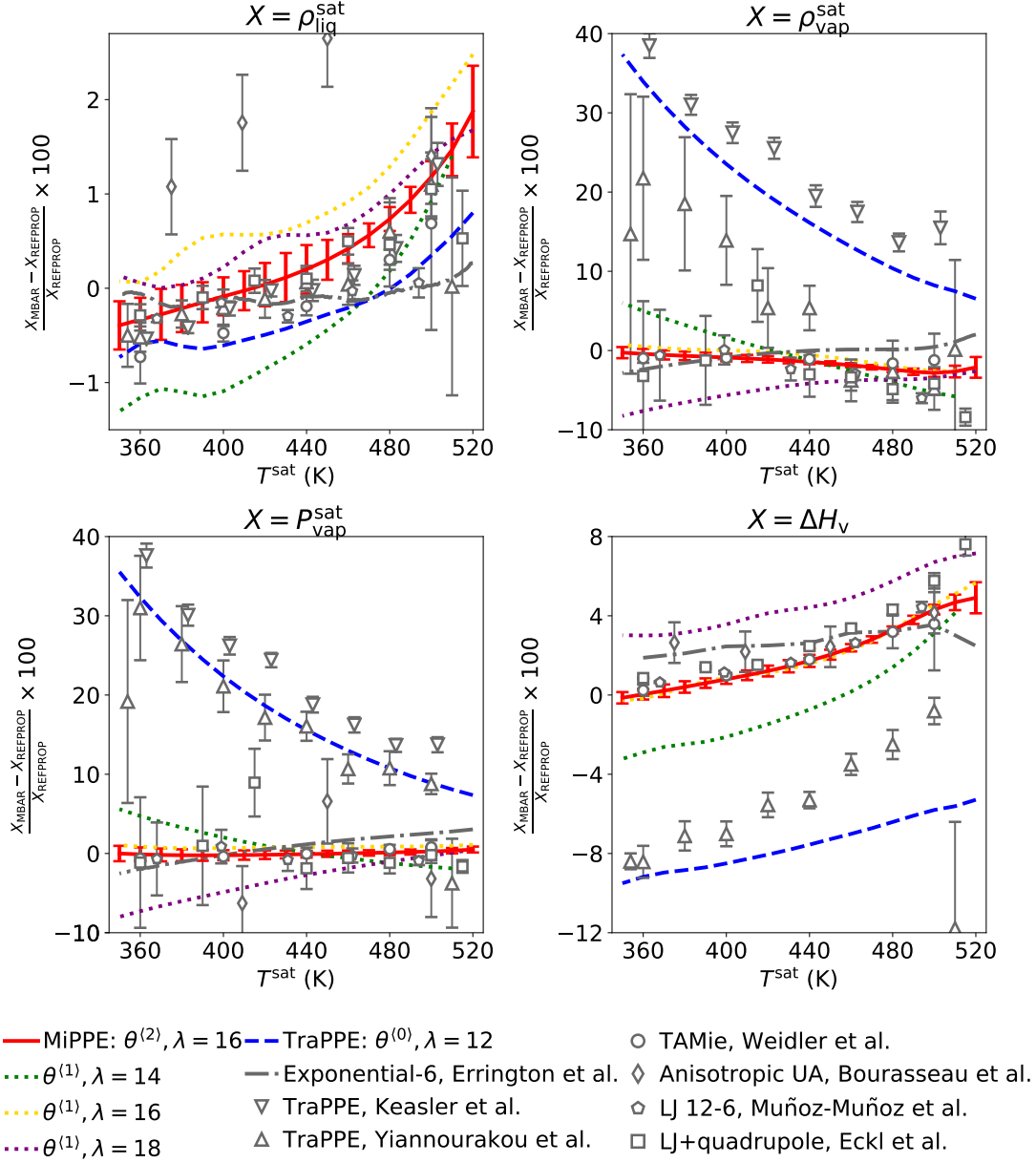


Figure 9: Percent deviations relative to REFPROP cyclohexane values<sup>55</sup> for MiPPE ( $\theta^{(2)}, \lambda_{\text{CH}_2} = 16$ ), zeroth iteration (TraPPE:  $\theta^{(0)}$ ), first iterations ( $\theta^{(1)}, \lambda_{\text{CH}_2} = 14, 16, 18$ ), and several literature force fields.<sup>22,24,27,56–59</sup> The first iteration parameter sets provide significant improvement compared to the zeroth iteration, while the second iteration (MiPPE) performs comparably to the most accurate literature force fields. Top-left, top-right, bottom-left, and bottom-right panels correspond to saturated liquid density, saturated vapor density, saturated vapor pressure, and enthalpy of vaporization, respectively. MiPPE uncertainties (95% confidence intervals) are obtained from 20 independent replicates. For clarity, the uncertainties for  $\theta^{(0)}$ ,  $\theta^{(1)}$ , and Errington et al.<sup>22</sup> are omitted.

Even the first iteration parameters demonstrate considerable improvement compared to the zeroth iteration (TraPPE) for predicting  $\rho_{\text{vap}}^{\text{sat}}$  and  $P_{\text{vap}}^{\text{sat}}$  without significantly diminishing the accuracy for  $\rho_{\text{liq}}^{\text{sat}}$  and  $\Delta H_v$ . In fact, the first iteration  $\lambda_{\text{CH}_2} = 16$  parameter set achieves similar deviations as the TAMie force field. The second (final) iteration provides further improvement in each property compared to the first iteration. In comparison with literature force fields, MiPPE (and TAMie) are arguably the most accurate at predicting  $\rho_{\text{vap}}^{\text{sat}}$ ,  $P_{\text{vap}}^{\text{sat}}$ , and  $\Delta H_v$ . With the exception of the Exponential-6,<sup>21</sup> MiPPE provides similar accuracy for  $\rho_{\text{liq}}^{\text{sat}}$  as the other literature force fields.

In this optimization example (an exhaustive 2-dimensional grid search over even integer values of  $\lambda_{\text{CH}_2}$ ), each proposed parameter set could be simulated directly in parallel. Therefore, the real time to solution for GCMC-MBAR would be similar to that of the GCMC-HR approach utilized by Mick et al.<sup>12</sup> and Soroush Barhaghi et al.,<sup>13</sup> although GCMC-MBAR would still reduce the total CPU time. In general, however, higher dimensional optimization algorithms are performed in sequence, where each iteration proposes new parameter set(s). In this scenario, GCMC-MBAR (with basis functions) is orders of magnitude faster than the literature GCMC-HR approach, which would require performing new GCMC simulations for each iteration.

In addition to requiring a more sophisticated optimization scheme, a higher dimensional parameterization would also necessitate generating more basis functions. Specifically, computing the overall system energy with basis functions requires an attractive and repulsive basis function for all  $ii$  (same) and  $ij$  (cross) pair interaction sets. For example, simultaneous optimization of the three united-atom site types in 2-methylbutane ( $\text{CH}_3$ ,  $\text{CH}_2$ , and  $\text{CH}$ ) would require both an attractive and repulsive basis function for each of the  $\text{CH}_3\text{-CH}_3$ ,  $\text{CH}_3\text{-CH}_2$ ,  $\text{CH}_3\text{-CH}$ ,  $\text{CH}_2\text{-CH}_2$ ,  $\text{CH}_2\text{-CH}$ , and  $\text{CH-CH}$  interactions. The additional computational overhead to compute more basis functions, however, is marginal.

## 4 Discussion

The results presented in this study were obtained by performing simulations with only a single reference force field. As shown in previous studies, a logical approach for improving the performance of MBAR is to include additional reference force fields.<sup>16,17</sup> For example, in Section 3.4, we did not utilize the snapshots from  $\lambda_{\text{CH}_2} = 14$  when computing properties for  $\lambda_{\text{CH}_2} = 16$  and vice versa. Using multiple reference force fields would certainly increase the number of effective snapshots. However, the top-left panel of Figure 7 demonstrates that a single reference provides sufficient overlap over a wide region of  $\epsilon$  and  $\sigma$  parameter sets when  $\lambda_{\text{rr}} = \lambda_{\text{ref}}$ . For this reason, we deemed it unnecessary to combine the snapshots from  $\theta^{(0)}$  and the four  $\theta^{(1)}$  reference simulations.

As molecular insertion moves are frequently rejected in high density systems, GCMC simulations are typically not reliable at low saturation temperatures ( $T^{\text{sat}} < 0.65T_c$ ). Because ITIC does not suffer from this low-temperature limitation, we recommend combining the MBAR-ITIC and GCMC-MBAR methods when predicting vapor-liquid coexistence properties from near-triple-point to near-critical-point conditions.

Although GCMC-HR is a standard approach for computing vapor-liquid coexistence, HR has also been applied to GEMC simulations (GEMC-HR).<sup>60</sup> Therefore, while the present study presents how MBAR can be applied to GCMC simulations, an analogous GEMC-MBAR approach is worth investigating in future work.

The main objective of GCMC-MBAR is similar to that of Hamiltonian scaling (HS), namely, to efficiently estimate phase equilibria properties for many force field parameter sets ( $\theta$ ) by maximizing the information content extracted from each simulation. Despite some apparent similarities between HS-GCMC and GCMC-MBAR, the means by which these two methods accomplish this objective are quite distinct. Both methods reweight from the mixture distribution of multiple  $\theta_{\text{ref}}$ .<sup>61</sup> The difference is that GCMC-MBAR gen-

erates this mixture distribution by combining configurations (or basis functions) sampled from independent simulations, while HS-GCMC samples directly from this mixture distribution in a single simulation and stores a combined (and scaled) histogram for each  $\theta_{\text{ref}}$ . To put it simply, HS-GCMC improves efficiency by modifying the sampling (simulation) approach, whereas GCMC-MBAR simply modifies the post-simulation data analysis (reweighting). Therefore, a possible synergy exists between the two methods by employing HS for sampling and MBAR for data analysis.

The present study has focused on the van der Waals Mie  $\lambda$ -6 non-bonded parameters ( $\epsilon$ ,  $\sigma$ , and  $\lambda$ ). However, GCMC-MBAR can also be applied to parameterize electrostatic non-bonded parameters, e.g., point charges ( $q$ ).<sup>46</sup> While the number of effective snapshots should still provide a reasonable estimate of reliability for  $q_{\text{rr}} \neq q_{\text{ref}}$ , we recommend that future work test the range of  $q_{\text{rr}}$  over which GCMC-MBAR is reliable.

## 5 Conclusions

This study demonstrates how the Multistate Bennett Acceptance Ratio (MBAR) can replace the traditional histogram reweighting approach for estimating vapor-liquid coexistence properties from grand canonical Monte Carlo simulations. MBAR and HR are mathematically equivalent in the limit of infinitesimal bin widths when the coexistence properties are computed for the reference force field. However, the primary benefit of MBAR is the ability to estimate properties for force fields that are not simulated directly, which greatly accelerates non-bonded parameterization.

We perform a one-dimensional  $\epsilon$ -scaling post-simulation optimization of several branched alkanes and alkynes. We provide empirical evidence that GCMC-MBAR is accurate when the number of effective snapshots is greater than fifty, which is typically the case in the vapor phase and in the liquid phase when  $\lambda_{\text{rr}} = \lambda_{\text{ref}}$ . We then show how GCMC-MBAR can

rapidly parameterize a family of Mie  $\lambda$ -6 potentials starting with a pre-tuned Lennard-Jones 12-6 potential (TraPPE). Specifically, with only two stages of direct GCMC simulation we consider hundreds of  $\epsilon_{\text{CH}_2}$ ,  $\sigma_{\text{CH}_2}$ , and  $\lambda_{\text{CH}_2}$  parameter sets. The optimized Mie 16-6 parameters for cyclohexane form the most recent contribution to the Mie Potentials for Phase Equilibria (MiPPE) force field.

## Acknowledgments

We would like to express our gratitude to Dr. J. Richard Elliott for several invaluable discussions regarding force field optimization. We are also appreciative of the internal review provided by Yauheni (Eugene) Paulechka, Andrei F. Kazakov, Daniel G. Friend, and Marcia L. Huber of the National Institute of Standards and Technology (NIST).

This research was performed while Richard A. Messerly held a National Research Council (NRC) Postdoctoral Research Associateship at NIST. Jeffrey J. Potoff and Mohammad Soroush Barhaghi acknowledge funding from NSF OAC-1642406. Some of the computations in this work were performed with resources from the Grid Computing initiative at Wayne State University.

Commercial equipment, instruments, or materials are identified only in order to adequately specify certain procedures. In no case does such identification imply recommendation or endorsement by NIST, nor does it imply that the products identified are necessarily the best available for the intended purpose.

Contribution of NIST, an agency of the United States government; not subject to copyright in the United States.

## Supporting information

Section S1 reports the bonded parameters. Section S2 compares phase equilibria for fixed and flexible bonds. Section S3 reports CBMC acceptance rates. Section S4 discusses hardware details. Section S5 provides the tabulated  $\epsilon$ -scaling results. Section S6 contains additional tabulated values and figures for the cyclohexane optimization. Section S7 depicts the compressibility factor of the vapor phase. Section S8 contains the tabulated values for the MBAR validation. Section S9 reports the simulation state points.

## References

- (1) Panagiotopoulos, A. Z. Monte Carlo methods for phase equilibria of fluids. *J. Phys.: Condens. Matter* **2000**, *12*, R25.
- (2) Stubbs, J. M.; Potoff, J. J.; Siepmann, J. I. Transferable Potentials for Phase Equilibria. 6. United-Atom Description for Ethers, Glycols, Ketones, and Aldehydes. *J. Phys. Chem. B* **2004**, *108*, 17596–17605.
- (3) Potoff, J. J.; Errington, J. R.; Panagiotopoulos, A. Z. Molecular simulation of phase equilibria for mixtures of polar and non-polar components. *Mol. Phys.* **1999**, *97*, 1073–1083.
- (4) Fern, J. T.; Keffer, D. J.; Steele, W. V. Measuring Coexisting Densities from a Two-Phase Molecular Dynamics Simulation by Voronoi Tessellations. *J. Phys. Chem. B* **2007**, *111*, 3469–3475.
- (5) Razavi, S. M.; Messerly, R. A.; Elliott, J. R. Coexistence Calculation Using the Isothermal-Isochoric Integration Method. *Fluid Ph. Equilibria* **2019**, *Pending publication*.

- (6) Martin, M. G.; Siepmann, J. I. Transferable potentials for phase equilibria. 1. United-atom description of n-alkanes. *J. Phys. Chem. B* **1998**, *102*, 2569–2577.
- (7) Hemmen, A.; Gross, J. Transferable Anisotropic United-Atom Force Field Based on the Mie Potential for Phase Equilibrium Calculations: n-Alkanes and n-Olefins. *J. Phys. Chem. B* **2015**, *119*, 11695–11707.
- (8) Potoff, J. J.; Bernard-Brunel, D. A. Mie Potentials for Phase Equilibria Calculations: Applications to Alkanes and Perfluoroalkanes. *J. Phys. Chem. B* **2009**, *113*, 14725–14731.
- (9) Ungerer, P.; Beauvais, C.; Delhommelle, J.; Boutin, A.; Rousseau, B.; Fuchs, A. H. Optimization of the anisotropic united atoms intermolecular potential for n-alkanes. *J. Chem. Phys.* **2000**, *112*, 5499–5510.
- (10) Messerly, R. A.; KnottsIV, T. A.; Wilding, W. V. Uncertainty quantification and propagation of errors of the Lennard-Jones 12-6 parameters for n-alkanes. *J. Chem. Phys.* **2017**, *146*, 194110.
- (11) Mick, J. R.; Soroush Barhaghi, M.; Jackman, B.; Rushaidat, K.; Schwiebert, L.; Potoff, J. J. Optimized Mie potentials for phase equilibria: Application to noble gases and their mixtures with n-alkanes. *J. Chem. Phys.* **2015**, *143*, 114504.
- (12) Mick, J. R.; Soroush Barhaghi, M.; Jackman, B.; Schwiebert, L.; Potoff, J. J. Optimized Mie Potentials for Phase Equilibria: Application to Branched Alkanes. *J. Chem. Eng. Data* **2017**, *62*, 1806–1818.
- (13) Soroush Barhaghi, M.; Mick, J. R.; Potoff, J. J. Optimised Mie potentials for phase equilibria: application to alkynes. *Mol. Phys.* **2017**, *115*, 1378–1388.

- (14) Chodera, J. D.; Swope, W. C.; Pitera, J. W.; Seok, C.; Dill, K. A. Use of the weighted histogram analysis method for the analysis of simulated and parallel tempering simulations. *J. Chem. Theory Comput.* **2007**, *3*, 26–41.
- (15) Shirts, M. R.; Chodera, J. D. Statistically optimal analysis of samples from multiple equilibrium states. *J. Chem. Phys.* **2008**, *129*, 124105.
- (16) Messerly, R. A.; Razavi, S. M.; Shirts, M. R. Configuration-Sampling-Based Surrogate Models for Rapid Parameterization of Non-Bonded Interactions. *J. Chem. Theory Comput.* **2018**, *14*, 3144–3162.
- (17) Messerly, R. A.; Shirts, M. R.; Kazakov, A. F. Uncertainty quantification confirms unreliable extrapolation toward high pressures for united-atom Mie  $\lambda$ -6 force field. *J. Chem. Phys.* **2018**, *149*, 114109.
- (18) Razavi, S. M. Optimization of a Transferable Shifted Force Field for Interfaces and Inhomogeneous Fluids using Thermodynamic Integration. M.Sc. thesis, The University of Akron, 2016.
- (19) Kiyohara, K.; Spyriouni, T.; Gubbins, K. E.; Panagiotopoulos, A. Z. Thermodynamic scaling Gibbs ensemble Monte Carlo: a new method for determination of phase coexistence properties of fluids. *Mol. Phys.* **1996**, *89*, 965–974.
- (20) Errington, J. R.; Panagiotopoulos, A. Z. Phase equilibria of the modified Buckingham exponential-6 potential from Hamiltonian scaling grand canonical Monte Carlo. *J. Chem. Phys.* **1998**, *109*, 1093–1100.
- (21) Errington, J. R.; Panagiotopoulos, A. Z. A new intermolecular potential model for the n-alkane homologous series. *J. Phys. Chem. B* **1999**, *103*, 6314–6322.



- (22) Errington, J. R.; Panagiotopoulos, A. Z. New intermolecular potential models for benzene and cyclohexane. *J. Chem. Phys.* **1999**, *111*, 9731–9738.
- (23) Martin, M. G.; Siepmann, J. I. Novel Configurational-Bias Monte Carlo Method for Branched Molecules. Transferable Potentials for Phase Equilibria. 2. United-Atom Description of Branched Alkanes. *J. Phys. Chem. B* **1999**, *103*, 4508–4517.
- (24) Keasler, S. J.; Charan, S. M.; Wick, C. D.; Economou, I. G.; Siepmann, J. I. Transferable Potentials for Phase Equilibria-United Atom Description of Five- and Six-Membered Cyclic Alkanes and Ethers. *J. Phys. Chem. B* **2012**, *116*, 11234–11246.
- (25) Nath, S. K.; Escobedo, F. A.; de Pablo, J. J. On the simulation of vapor-liquid equilibria for alkanes. *J. Chem. Phys.* **1998**, *108*, 9905–9911.
- (26) Nath, S. K.; Khare, R. New forcefield parameters for branched hydrocarbons. *J. Chem. Phys.* **2001**, *115*, 10837–10844.
- (27) Yiannourakou, M.; Ungerer, P.; Lachet, V.; Rousseau, B.; Teuler, J.-M. United atom forcefield for vapor-liquid equilibrium (VLE) properties of cyclic and polycyclic compounds from Monte Carlo simulations. *Fluid Ph. Equilibria* **2019**, *481*, 28 – 43.
- (28) Transferable Potentials for Phase Equilibria. 2019; <http://chem-siepmann.oit.umn.edu/siepmann/trappe/index.html>, Date accessed: February 25, 2019.
- (29) Allen, M. P.; Tildesley, D. J. *Computer simulation of liquids*; Clarendon Press ; Oxford University Press: Oxford England New York, 1987; pp xix, 385 p.
- (30) Nezbeda, I. Simulations of Vapor-Liquid Equilibria: Routine versus Thoroughness. *J. Chem. Eng. Data* **2016**, *61*, 3964–3969.

- (31) Shah, J. K.; Maginn, E. J. A general and efficient Monte Carlo method for sampling intramolecular degrees of freedom of branched and cyclic molecules. *J. Chem. Phys.* **2011**, *135*, 134121.
- (32) Baumgärtner, A.; Binder, K. Monte Carlo studies on the freely jointed polymer chain with excluded volume interaction. *J. Chem. Phys.* **1979**, *71*, 2541–2545.
- (33) Nejahi, Y.; Barhaghi, M. S.; Mick, J.; Jackman, B.; Rushaidat, K.; Li, Y.; Schwiebert, L.; Potoff, J. GOMC: GPU Optimized Monte Carlo for the simulation of phase equilibria and physical properties of complex fluids. *SoftwareX* **2019**, *9*, 20 – 27.
- (34) Martínez, L.; Andrade, R.; Birgin, E. G.; Martínez, J. M. PACKMOL: A package for building initial configurations for molecular dynamics simulations. *J. Comput. Chem.* **2009**, *30*, 2157–2164.
- (35) Humphrey, W.; Dalke, A.; Schulten, K. VMD: Visual molecular dynamics. *J. Mol. Graphics* **1996**, *14*, 33 – 38.
- (36) Ferrenberg, A. M.; Swendsen, R. H. New Monte Carlo technique for studying phase transitions. *Phys. Rev. Lett.* **1988**, *61*, 2635–2638.
- (37) Ferrenberg, A. M.; Swendsen, R. H. Optimized Monte Carlo data analysis. *Phys. Rev. Lett.* **1989**, *63*, 1195–1198.
- (38) McDonald, I. R.; Singer, K. Machine Calculation of Thermodynamic Properties of a Simple Fluid at Supercritical Temperatures. *J. Chem. Phys.* **1967**, *47*, 4766–4772.
- (39) Card, D. N.; Valleau, J. P. Monte Carlo Study of the Thermodynamics of Electrolyte Solutions. *J. Chem. Phys.* **1970**, *52*, 6232–6240.
- (40) Wood, W. W. Monte Carlo Calculations for Hard Disks in the Isothermal-Isobaric Ensemble. *J. Chem. Phys.* **1968**, *48*, 415–434.

- (41) Kumar, S.; Rosenberg, J. M.; Bouzida, D.; Swendsen, R. H.; Kollman, P. A. THE weighted histogram analysis method for free-energy calculations on biomolecules. I. The method. *J. Comput. Chem.* **1992**, *13*, 1011–1021.
- (42) Souaille, M.; Roux, B. Extension to the weighted histogram analysis method: combining umbrella sampling with free energy calculations. *Comput. Phys. Commun.* **2001**, *135*, 40 – 57.
- (43) Duarte Ramos Matos, G.; Kyu, D. Y.; Loeffler, H. H.; Chodera, J. D.; Shirts, M. R.; Mobley, D. L. Approaches for Calculating Solvation Free Energies and Enthalpies Demonstrated with an Update of the FreeSolv Database. *J. Chem. Eng. Data* **2017**, *62*, 1559–1569.
- (44) Efron, B. Bootstrap Methods: Another Look at the Jackknife. *Ann. Stat.* **1979**, *7*, 1–26.
- (45) Messerly, R. A.; Rowley, R. L.; KnottsIV, T. A.; Wilding, W. V. An improved statistical analysis for predicting the critical temperature and critical density with Gibbs ensemble Monte Carlo simulation. *J. Chem. Phys.* **2015**, *143*, 104101.
- (46) Naden, L. N.; Shirts, M. R. Rapid Computation of Thermodynamic Properties Over Multidimensional Nonbonded Parameter Spaces using Adaptive Multistate Reweighting. *J. Chem. Theory Comput.* **2016**, *12*, 1806–1823.
- (47) Dybeck, E. C.; König, G.; Brooks, B. R.; Shirts, M. R. Comparison of Methods To Reweight from Classical Molecular Simulations to QM/MM Potentials. *J. Chem. Theory Comput.* **2016**, *12*, 1466–1480.
- (48) Weidler, D.; Gross, J. Individualized force fields for alkanes, olefins, ethers and ketones based on the transferable anisotropic Mie potential. *Fluid Ph. Equilibria* **2018**,

- (49) Rowley, R. L.; Wilding, W. V.; Oscarson, J. L.; KnottsIV, T. A.; Giles, N. F. *DIPPR Data Compilation of Pure Chemical Properties*; Design Institute for Physical Properties; AIChE: New York, NY, 2013.
- (50) Lemmon, E. W.; Bell, I. H.; Huber, M. L.; McLinden, M. O. NIST Standard Reference Database 23: Reference Fluid Thermodynamic and Transport Properties-REFPROP, Version 10.0, National Institute of Standards and Technology. 2018; <https://www.nist.gov/srd/refprop>, Date accessed: June 21, 2018.
- (51) Lemmon, E. W.; Span, R. Short Fundamental Equations of State for 20 Industrial Fluids. *J. Chem. Eng. Data* **2006**, *51*, 785–850.
- (52) Blackham, T.; Lemmon, A.; Lemmon, E. Fundamental Equation of State for Isooctane. *Int. J. Thermophys.* **2018**, *Pending publication*.
- (53) Gao, K.; Wu, J.; Lemmon, E. **2017**, *Unpublished equation*.
- (54) Polt, A.; Platzer, B.; Mauer, G. Parameter der Thermischen Zustandsgleichung von Bender fuer 14 Mehroatomige Reine Stoffe. *Chem. Tech. (Leipzig, Ger.)* **1992**, *44*.
- (55) Zhou, Y.; Liu, J.; Penoncello, S. G.; Lemmon, E. W. An Equation of State for the Thermodynamic Properties of Cyclohexane. *J. Phys. Chem. Ref. Data* **2014**, *43*, 043105.
- (56) Weidler, D.; Gross, J. Transferable Anisotropic United-Atom Force Field Based on the Mie Potential for Phase Equilibria: Aldehydes, Ketones, and Small Cyclic Alkanes. *Ind. Eng. Chem. Res.* **2016**, *55*, 12123–12132.
- (57) Eckl, B.; Vrabec, J.; Hasse, H. Set of Molecular Models Based on Quantum Mechanical Ab Initio Calculations and Thermodynamic Data. *J. Phys. Chem. B* **2008**, *112*, 12710–12721.

- (58) Bourasseau, E.; Ungerer, P.; Boutin, A. Prediction of Equilibrium Properties of Cyclic Alkanes by Monte Carlo Simulation-New Anisotropic United Atoms Intermolecular Potential-New Transfer Bias Method. *J. Phys. Chem. B* **2002**, *106*, 5483–5491.
- (59) Muñoz-Muñoz, Y. M.; Guevara-Carrion, G.; Llano-Restrepo, M.; Vrabec, J. Lennard-Jones force field parameters for cyclic alkanes from cyclopropane to cyclohexane. *Fluid Ph. Equilibria* **2015**, *404*, 150 – 160.
- (60) Boulougouris, G. C.; Peristeras, L. D.; Economou, I. G.; Theodorou, D. N. Predicting fluid phase equilibrium via histogram reweighting with Gibbs ensemble Monte Carlo simulations. *J. Supercrit. Fluids* **2010**, *55*, 503 – 509, 100th year Anniversary of van der Waals' Nobel Lecture.
- (61) Shirts, M. R. Reweighting from the mixture distribution as a better way to describe the Multistate Bennett Acceptance Ratio. <https://arxiv.org/abs/1704.00891>